



Contents lists available at ScienceDirect

# International Journal of Applied Earth Observations and Geoinformation

journal homepage: [www.elsevier.com/locate/jag](http://www.elsevier.com/locate/jag)

## Explaining Sentinel 2-based dNBR and RdNBR variability with reference data from the bird's eye (UAS) perspective

Fabian Ewald Fassnacht<sup>a,\*</sup>, Ephraim Schmidt-Riese<sup>a</sup>, Teja Kattenborn<sup>a,b</sup>, Jaime Hernández<sup>c</sup><sup>a</sup> Karlsruhe Institute of Technology, Institute of Geography and Geoecology, Kaiserstraße 12, 76131 Karlsruhe, Germany<sup>b</sup> Remote Sensing Center for Earth System Research, University of Leipzig, Talstr. 35, 04103 Leipzig, Germany<sup>c</sup> Universidad de Chile, Forestry and Nature Conservation Faculty, GEP, Santa Rosa 11315, Santiago de Chile, Chile

## ARTICLE INFO

## Keywords:

UAS  
dNBR variability  
Wildfire  
Sentinel-2  
RdNBR  
Shadows

## ABSTRACT

Characterizing the spatial variability of the severity of wildfires is important to assess ecological and economic consequences and to coordinate mitigation strategies. Vegetation indices such as the differenced Normalized Burn Ratio (dNBR) have become a standard tool to assess burn or fire severity across larger areas and are being used operationally. Despite the frequent application of dNBR-like vegetation indices, it is not yet fully understood which variables exactly drive the variability in dNBR observed by multispectral satellites. One reason for this is the lack of high quality prefire information about vegetation structure and composition. Consequently, the influence of prefire vegetation composition and other potentially influential variables such as cast shadows has hardly been examined. Here, we use very high resolution Unmanned Aerial System (UAS) orthoimages collected briefly before and after the large wildfires in Central Chile in the fire season 2016/2017 to derive variables related to the pre- and postfire landscape composition and structure. The variables are used as predictors in Generalized Additive Models (GAM) to explain the spatial variability in dNBR and RdNBR pixel values as observed by Sentinel-2. Our models explain more than 80% and 75% of the variability in dNBR and RdNBR values, respectively, using a sparse set of five predictors. The results suggest that in our study area the largest fraction of variability in Sentinel-2 based dNBR and RdNBR values can be explained by variables related to the fraction of consumed canopy cover while the vegetation composition before the fire does not have a large influence on dNBR and RdNBR.

Our results further suggest that cast-shadows of snags and standing dead trees with remaining crown structure have a notable influence on the dNBR signal which may have been underestimated so far. We conclude that spatially continuous, very high spatial resolution data from UAS can be a valuable data source for an improved understanding of the exact meaning of common vegetation index products, operationally used for monitoring the environment.

### 1. Introduction

Wildfires are an integral part of many ecosystems, shaping their structure and functions (Attiwill, 1994) and having significant global impacts on terrestrial, aquatic and atmospheric systems (Lentile et al., 2006). Wildfire occurrences and intensity are increasing in many parts of the world due to human activities (e.g., Balch et al., 2017) and climate warming (Harvey et al., 2019; Westerling, 2016). Understanding wildfires is of high scientific interest because wildfires are a hazard to human properties and life (Cohen, 2000) and because of the manifold ways wildfires affect ecosystems and ecosystem services. This includes effects

on water provision (e.g., Hallema et al., 2017; Spencer et al., 2003) erosion protection (e.g., Ice et al., 2004; Robichaud et al., 2020) and carbon storage (e.g., Liu et al., 2014; North & Hurteau, 2011).

Wildfires often affect large and remote areas with at least partly limited accessibility. Hence, remote sensing approaches have been an effective tool for mapping and characterizing wildfires and their effects for many years. Studies suggested methods to map fire scars at local (e.g., Kasischke et al., 1992; Nioti et al., 2011) to regional (e.g., Bourgeau-Chavez et al., 1997; Pu et al., 2004) and even global scales (e.g., Alonso-Canas & Chuvieco, 2015; Giglio et al., 2006) using mostly airborne and spaceborne multispectral and Radar data in combination with simple

\* Corresponding author at: Karlsruhe Institute of Technology, Institute of Geography and Geoecology, Kaiserstraße 12, 76131 Karlsruhe, Germany.

E-mail address: [fabian.fassnacht@kit.edu](mailto:fabian.fassnacht@kit.edu) (F.E. Fassnacht).

<https://doi.org/10.1016/j.jag.2020.102262>

Received 28 August 2020; Received in revised form 15 October 2020; Accepted 22 October 2020

Available online 10 November 2020

0303-2434/© 2020 The Authors. Published by Elsevier B.V. This is an open access article under the CC BY license (<http://creativecommons.org/licenses/by/4.0/>).

thresholding procedures or more complex classification approaches. Such approaches often achieve very high accuracies when compared to visually delineated fire scars and field-reference data and are nowadays used operationally (Hua & Shao, 2017). Remote sensing has also been used to characterize the fire or burn severity patterns in fire affected areas. This is relevant as fires often burn heterogeneously in a landscape due to variable availability of fuel material as well as topographic and weather differences (Cocke et al., 2005 and references therein, Viedma et al., 2020, Whitman et al., 2018). To assess and understand the ecological and economic consequences and risks of a given wildfire and coordinate corresponding management activities, accurately mapping the variability in fire or burn severity is desirable (Whitman et al., 2018). However, relating the remotely sensed information about fire or burn severity to the actual processes and changes that occurred on the ground remains challenging (Lentile et al., 2009). In this context, the terms fire severity and burn severity have been subject to wide discussions as their definition is sometimes fuzzy and both terms are used in many different contexts in the remote sensing literature (Lentile et al., 2006). Lentile et al. (2006) defines “fire severity” as a measure that describes short-term impacts of fire on an environment (e.g., consumption of organic material and tree mortality, charcoal decomposition, etc.) while “burn severity” describes long-term ecological changes introduced to a landscape through a fire and the corresponding ecosystem responses (e.g., delayed tree mortality, vegetation resprouting, re-colonization with vegetation) (Cansler & McKenzie, 2012). Hence, remote sensing data depicting situations after a wildfire may contain information on both “burn severity” and “fire severity” depending also on how long after the fire the data are acquired. It is further important that the meaning of both terms may vary drastically depending on the examined ecosystem and neither of them is generally (per definition) connected to defined measurable ecological variables, even though this may be the case in individual studies.

In the remote sensing literature, the most common approaches to characterize fire and burn severity base on spectral indices (e.g., Key & Benson, 2006), spectral unmixing (Lentile et al., 2009; Veraverbeke & Hook, 2013) and radiative transfer models (Chuvieco et al., 2007; García et al., 2020) applied to multispectral or hyperspectral data. All these approaches make use of the fact that wildfires alter the optical properties of most elements of natural landscapes and particularly vegetation and soil. In summary, wildfires typically cause a general drop in reflectance in the visual (VIS)-near infrared (NIR) region due to vegetation removal and transformation of vegetation material to charcoal. However, the magnitude of the drop may vary notably depending on the prefire vegetation status with moist vegetation typically showing smaller drops in reflectance than dry vegetation which typically has higher prefire reflectance. The drops in reflectance are normally consistent in the NIR while the VIS region shows more variable changes depending on the prefire land-cover (Maier, 2010). Only subtle drops or even reflectance increases have been observed for the shortwave infrared (SWIR) region (Key & Benson, 2006; White et al., 1996). This is most likely connected to reduced foliage and hence leaf water absorption in the SWIR. Furthermore, white ash depositions may lead to short-term increases in reflectance throughout the VIS-SWIR range (Roy & Landmann, 2005) but these depositions typically disappear within a short time-window after the fire.

The fact that NIR and SWIR reflectance are oppositely affected by fires is exploited by several spectral indices. These are at the same time the most widely studied approach to map fire and burn severity-related spectral variability. Among these indices, the differenced Normalized Burn Ratio (dNBR) and some derivations of it have become a standard procedure for rapidly assessing spectral fire effects. The NBR is calculated as the normalized difference of a band covering the NIR (0.76–0.90  $\mu\text{m}$ ) and a band covering the SWIR (2.08–2.35  $\mu\text{m}$ ). dNBR is

then derived by subtracting a postfire NBR image from the prefire NBR image. Numerous studies have examined in which way the dNBR represents field-measured burn severity metrics (e.g., Cansler & McKenzie, 2012; Cocke et al., 2005; Harvey et al., 2019). The latter were often acquired using the Composite Burn Index (CBI) or the GeoCBI protocol suggested by Key & Benson (2006) and De Santis & Chuvieco, (2009), respectively. The CBI is a rapid and standardized semi-quantitative visual interpretation-based field approach to summarize ecological relevant effects of wildfires on vegetation and soil observed in five (height-related) strata into a single site index (Cansler & McKenzie, 2012; French et al., 2008). The GeoCBI builds on the concept of the CBI but additionally integrates the fractional cover of each considered strata to improve the relation on the index with the remote sensing signal (Cansler & McKenzie, 2012). While CBI data was found to show good correlations with dNBR at the sites for which it was developed (Key & Benson, 2006), other studies showed that the strength of the relationship between dNBR and CBI and GeoCBI depends on the studied ecosystem and may be weak in some ecosystems or sites (French et al., 2008).

One of the advantages of the CBI concept - its relative simplicity which allows a rapid data collection in the field - is also a major weakness for at least two reasons: 1. The CBI assessments have been criticized to be partly subjective and 2. by integrating all ecological relevant fire effects into a single index number, it is hard to understand which changes on the surface induced by the wildfire are actually driving the observed spectral changes (Harvey et al., 2019; Morgan et al., 2014). The fact that CBI measurements are collected in plots on the ground (and hence do not share the bird-eye perspective of the remote sensing data) and are not spatially continuous further complicates their linkage to remotely sensed indices such as the dNBR. Understanding the fire-induced changes on the environment, which led to the observed remote sensing signal, in ideal case, requires spatially continuous information about the vegetation composition and structure as well as the spatial landscape patterns before and after the fire. Some studies reconstructed such information from postfire field surveys in larger plots. For example, Harvey et al. (2019) related dNBR measurements from a large geographical gradient to reconstructed prefire stand structure variables, topography and prefire bark beetle activity. They found a notable influence of these variables on the observed dNBR values and suggested that particularly in the presence of a large variability of forest structures, differences in dNBR values may not only represent differences in fire or burn severity. In a comparable study, Miller et al. (2009) related percentage canopy cover change and percentage basal area change with RdNBR values and found good correlations. McCarley et al. (2017) had prefire and postfire LiDAR data available and examined how changes in forest structure relate to spectral fire effects observed by Landsat. They found a high correlation between LiDAR-derived canopy cover change and the ratio of Landsat band 7 and 4 – the same bands used to calculate dNBR. They found a general trend that structural metrics calculated for the upper part of the canopy related better to the Landsat-observed spectral changes. A stronger relation of dNBR with canopy changes than with surface fuel reduction has also been reported in other studies (e.g., Harvey et al., 2019; Hoy et al., 2008). Wulder et al. (2009) also examined pre- and postfire LiDAR data and observed that vegetation fill (a LiDAR-based representation of the height and density of vegetation), postfire and absolute change in crown closure as well as relative change in average canopy height are useful for characterizing postfire spectral changes as observed by dNBR and related spectral indices.

Similar to canopy cover and other measures of vegetation density, the vegetation type or species as well as the fraction of shadows may also influence postfire spectral changes. Vegetation types and species vary notably in terms of their greenness (pigments) as well as their reflectance amplitude in the NIR and SWIR region (differing canopy and leaf

structures and water contents) (Kattenborn et al., 2019a; Kattenborn and Schmidtlein, 2019). The latter should hence also have an influence on the dNBR. To address this issue, Miller & Thode (2007) suggested a modification to the dNBR, the so called relative dNBR (RdNBR). The RdNBR normalizes the dNBR with the square root of the prefire NBR to account for prefire variability in vegetation composition.

Further, shadows within and between tree crowns and vegetation canopies can largely influence the spectral signal. In a postfire forest landscape, standing snags may lead to a notable fraction of shaded ground that influence the passive optical satellite signals and may affect the dNBR signal. The potential influence of shadow casts by trees has been discussed with respect to differing solar elevation angles for satellite data acquisitions (Hoy et al., 2008) but may also be a more general problem related to, for example, the density of snags after the fire. It is unlikely that the normalization procedure of the RdNBR will mitigate the influence of shadows of snags as they did not exist in this way in the prefire signal.

The role of vegetation shadows as well as the influence of prefire vegetation composition on the observed dNBR variability has not been widely examined, yet. The few studies that addressed these issues typically based on re-constructed information from postfire plot-based field work and had no spatially continuous and highly resolved information about the vegetation composition available (e.g., Miller et al., 2009; Whitman et al., 2018). Such information may now increasingly become available through unmanned aerial systems (UAS) data, collected before wildfire incidents.

Here, we examine how dNBR and RdNBR signals retrieved from Sentinel-2 data relate to pre- and postfire vegetation structure and composition as well as shadows in a diverse Mediterranean landscape in South-Central Chile. We extract information about the pre- and postfire vegetation situation from two UAS surveys conducted briefly before and after the wildfires occurring during the Southern summer of 2016/2017. The UAS surveys allow us to work with a comparably high number of

samples, also from areas which are hardly accessible in the field. With this approach we aim on creating an improved understanding of the main drivers of the dNBR variability in Mediterranean landscapes.

## 2. Methods

### 2.1. Study sites

The study region is located in Central Chile in the southeast of the city Constitución, province of Maule. The climate in the Maule region is Mediterranean with warm-dry summers and cold-wet winters. It is classified as “Csb” in the Koeppen classification scheme (Kottek et al., 2006). Fire occurrence during summer is common (CONAF, 2017) but the number of ignitions and total area burnt depends strongly on inter-annual climate variability (González et al., 2005; Urrutia-Jalabert et al., 2018). Wildfires are intensified by high precipitation in fall and winter, inducing biomass accumulation. Even more influential is the degree of summer drought (Urrutia-Jalabert et al., 2018).

In the time period between December 2016 and February 2017 vast wildfires occurred in Central Chile and destroyed over 5,000 km<sup>2</sup> of forested areas. 93% of the fires occurred between 1st of January and 10th of February. In the Maule region, about 54% of the total area was burnt (CONAF, 2017). Prolonged drought and unusual high temperatures have led to this devastating wildfire season. Most fires started on 18th of January. Some fires merged and grew critically on the 25th of January and lasted in high intensities until the 5th of February 2017. A detailed summary of the wildfires of this season is provided by de la Barrera et al. (2018).

Our local sites covered with UAS data (Fig. 1) were distributed in the surroundings of the city Constitución. The study sites are dominated by dense forests (coverage > 80%) with a low proportion of shrubland (Matorral). The investigated forest areas consisted mainly of native vegetation or native forests mixed with *Pinus radiata* individuals while

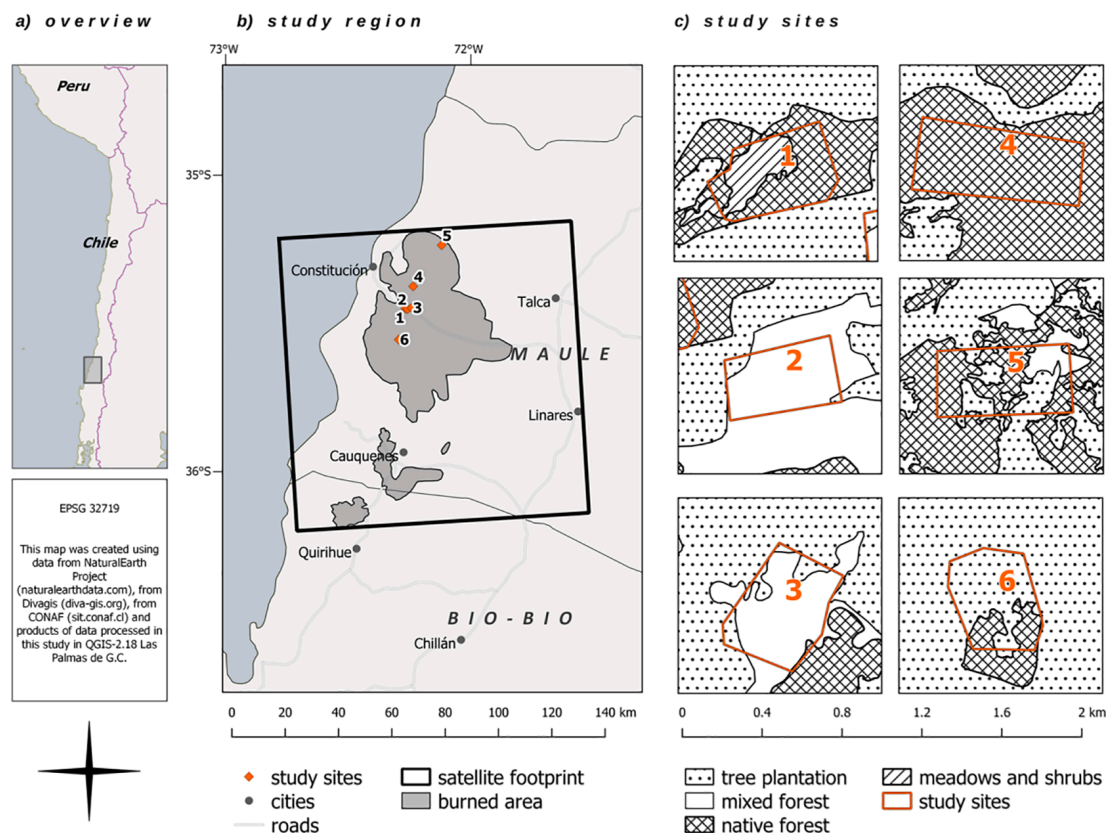


Fig. 1. Our analysis includes six subsites inside the satellite footprint (b). The study sites cover mixed and natural forests as well as tree plantations (c).

the perimeter of the local sites were often covered by tree plantations which cover a large proportion of the total area of the Maule region. Within our six sites the forests consisted mainly of *Nothofagus glauca* a vulnerable endemic species (IUCN, 2017), some sclerophyll species (*Quillaja saponaria*, *Maytenus boaria*, *Cryptocarya alba*) and *Pinus radiata*, the non-native though most common plantation tree in Chile (GERENCIA FORESTAL, 2011). At sites 1 to 4 the fire was intense and no or hardly any vegetation survived, whereas on sites 5 and 6 notable proportions of green vegetation remained after the fire.

## 2.2. Data acquisition and pre-processing

### 2.2.1. Satellite data

We used Sentinel-2 data to calculate dNBR and RdNBR with a resolution of 20 m. We focused on dNBR and RdNBR as these are amongst the most frequently applied indices to assess burned areas in satellite images. We did not consider additional related indices such as the Relativized Burn Ratio (RBR) as we found it to be highly correlated (0.95 and 0.99, respectively) to dNBR and RdNBR and hence did not expect any additional insights from repeating the analyses for these indices. We acquired L1C-tiles of Sentinel-2 data via the EarthExplorer (earthexplorer.usgs.gov) website. We used satellite images with acquisition dates as close as possible to the corresponding UAS acquisition dates to avoid potential effects of changes occurring after the UAS acquisitions (Table 1). On the selected images our study sites were cloudless. An atmospheric correction was performed using the standalone version of the Sen2Cor-Processor (ESA) (Mousivand et al., 2015). Using Sentinel's Application Platform (SNAP), we resampled all bands to 20 m pixel size using bilinear resampling. We used band 8a (NIR with band center at 865 nm) and band 12 (SWIR with band center at 2190 nm) to calculate the dNBR and the RdNBR according to Eqs. (1)–(3):

$$\text{NBR} = (\text{NIR} - \text{SWIR}) / (\text{NIR} + \text{SWIR}) \quad (1)$$

$$\text{dNBR} = \text{NBR}_{\text{prefire}} - \text{NBR}_{\text{postfire}} \quad (2)$$

$$\text{RdNBR} = \text{dNBR} / \text{abs}(\text{NBR}_{\text{prefire}})^{0.5} \quad (3)$$

No expansive land-cover changes occurred in the areas covered by the UAS images during the time period between the pre-fire image acquisition (5th March 2016) and the start of the wildfires (December 2016).

### 2.2.2. Unmanned aerial systems (UAS) surveys

We used UAS imagery to obtain information about pre- and postfire vegetation composition, structure and shadows. The prefire and postfire UAS surveys were conducted in March 2016 and April 2017, respectively (Table 1). We used an octocopter carrying a Canon EOS 100D camera to take between 200 and 400 pictures at each site at an altitude of about 200 m. From the Red Green Blue (RGB) imagery, we derived orthoimagery and obtained height information from photogrammetric point clouds. We applied the standard processing chain implemented in Agisoft Photoscan (version 1.4.0.5650) as described in full detail in Supplementary Material 1. The images were automatically georeferenced using the GPS trajectories of the drone. For each subarea, we additionally co-registered the pre- to the postfire image to improve the precision of the spatial overlay. For this we selected between 12 and 20 control points on each study site. We cut off a margin of about 100 m

**Table 1**  
Acquisition dates of UAS and Sentinel-2 data.

Dataset	Acquisition date
Prefire UAS survey	11th–21st of March 2016
Prefire Sentinel-2 image	5th of March 2016
Postfire UAS survey	10th and 13th of April 2017
Postfire Sentinel-2 image	29th of April 2017

from the borders of each orthomosaic to exclude blurry parts of the mosaics. This processing resulted in an aggregated study area of about 113 ha equivalent to 2.828 Sentinel-2 pixels (20 × 20 m pixel size). The final ortho-images had a pixel size of 3 cm.

### 2.2.3. Deriving vegetation structure information from the UAS data

From the photogrammetric point cloud derived with the Agisoft processing chain, we calculated a Digital Surface Model (DSM) and a Digital Terrain Model (DTM). We used the prefire point cloud to derive a DSM with 0.5 m pixel size using the DSM algorithm in the TreesVis software (Weinacker et al., 2004). Contrarily, we used the postfire point cloud data to calculate a DTM with 2 m pixel size using the DTM algorithm in TreesVis. We applied the postfire point cloud to derive the DTM as a notably larger proportion of the ground was visible after most of the vegetation canopies had been burned. After downsampling the DTM to the pixel size of the DSM we calculated a canopy height model representing the situation before the fire by subtracting the DTM from the DSM.

### 2.2.4. Pre- and postfire vegetation composition and landscape structure

Information on pre- and postfire vegetation composition and landscape structure was derived by classifying the UAS ortho-images into major vegetation types as well as shadow and non-vegetated areas using a supervised classification. In the prefire image we defined three vegetation types including “Pinus radiata”, “Nothofagus” and “Sclerophyll”. The “Nothofagus” class mostly consisted of *Nothofagus glauca* (hualo), and *Nothofagus caducifolia* while the “Sclerophyll” class summarized a range of sclerophyll species including for example *Quillaja saponaria*, *Maytenus boaria* and *Cryptocarya alba*. These three vegetation types clearly differed in their optical traits showing distinct shades of green in the ortho-images (Fig. 2). Besides the three vegetation types we considered the classes “non vegetation”, “shadow” and “dry vegetation”. For the postfire image we differentiated the classes “non vegetation”, “shadow”, “singed vegetation” and “green vegetation”. The postfire class “green vegetation” summarizes all vegetation types as the overall fraction of living vegetation was small after the fire and it would have been impossible to reach a meaningful sample size for the three vegetation types. The postfire class “singed vegetation” includes all non-green postfire vegetation with leaves present. The class “non vegetation” includes bare soil, roads, woody residues, and rocks (see also Figs. 10–12). For each site we collected a total of 272 to 1721 training samples using visual interpretation (Table 2). We tried to collect at least 50 samples for each considered class and UAS dataset. In some cases this was not possible because some classes only occurred marginally in some of the UAS datasets. However, the applied Support Vector machines (SVM) classifier (see below) is known to perform well with sparse training samples (Mountrakis et al., 2011).

We augmented the feature space derived from the UAS imagery by adding four grey level co-occurrence (GLCM) texture parameters (homogeneity, variance, entropy and correlation) in two resolutions (1 m and 2 m). This resulted in 11 features as input to the supervised classification (RGB + 2 × 4 texture parameters). We applied a Support Vector Machines (SVM) classifier using a Radial Basis Function (RBF) as kernel function (Hsu et al. 2003). For the RBF parameters sigma and cost we determined optimal values using a grid-search (Hsu et al., 2003; Kuhn, 2013). Further details can be found in the R-Documentation for the e1071-package (Meyer et al., 2017). We evaluated the resulting SVM models using a 5-fold cross-validation (Hsu et al., 2003; Kuhn, 2013). We selected SVM as classifier based on the good performances we obtained with it in earlier studies using UAS-like data (Lopatin et al., 2017) and based on its superiority in method comparison studies focusing on the classification of vegetation (e.g., Fassnacht et al., 2014).

First results showed that the classes “dry vegetation” and “singed vegetation” interfered notably with the “non vegetation” class in some areas. Hence, we decided to re-classify “dry vegetation” below 2 m to “non vegetation” using the height information of the nDSM. This step

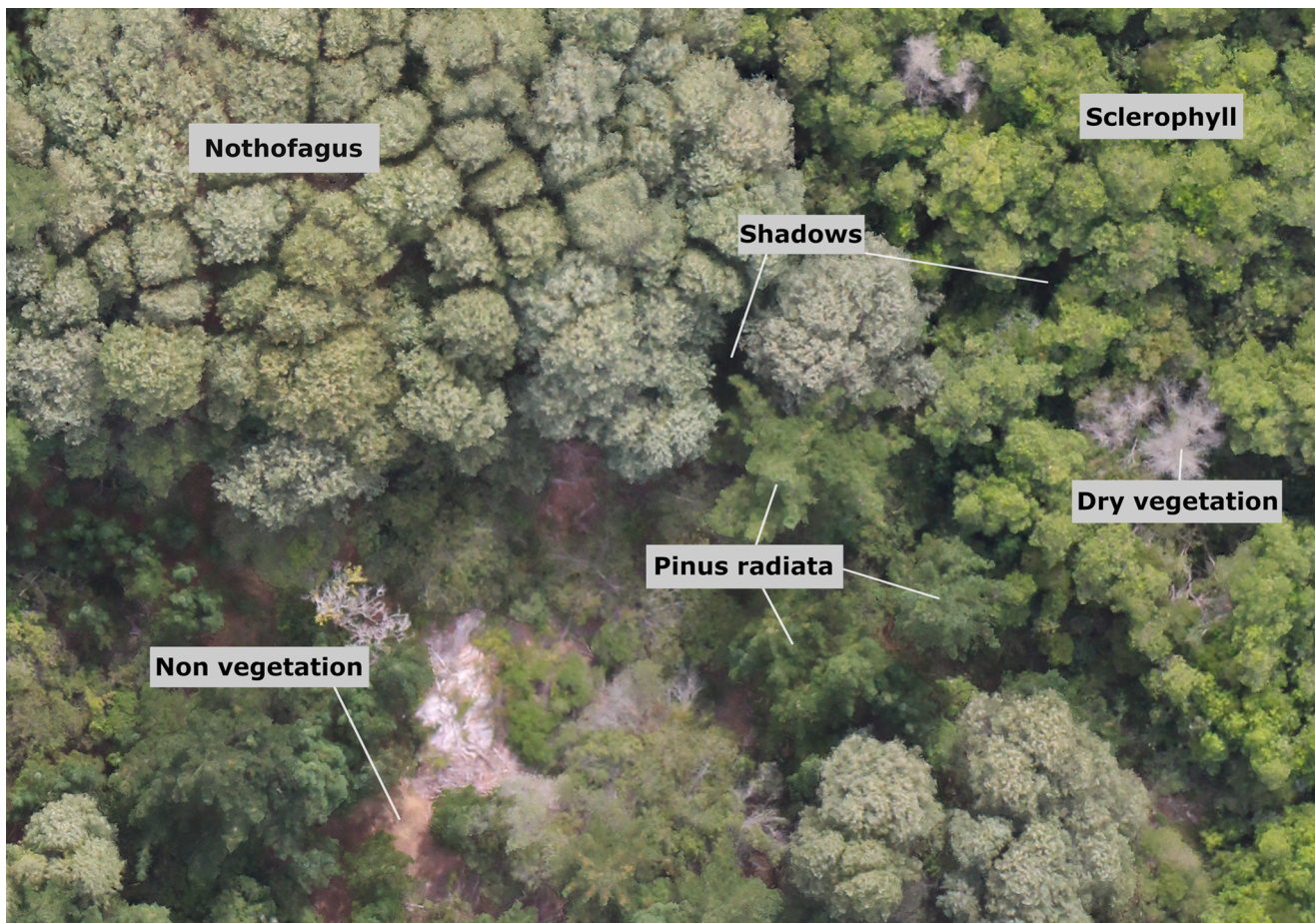


Fig. 2. Examples of the six land-cover classes considered in the prefire data.

**Table 2**  
Number of sample plots per class and flight. Prefire and Postfire classifications were conducted separately.

Class	Site 1	Site 2	Site 3	Site 4	Site 5	Site 6
Prefire non vegetation	382	153	200	33	361	120
Prefire Sclerophyll	128	57	116	193	100	16
Prefire Pinus radiata	310	164	325	190	193	176
Prefire Nothofagus	406	134	426	696	306	172
Prefire dry vegetation	130	58	22	98	17	21
Prefire shadow	76	114	85	73	53	50
Postfire non vegetation	170	729	359	209	1058	145
Postfire green vegetation	26	134	100	20	233	92
Postfire singed vegetation	46	201	207	79	252	54
Postfire shadow	30	268	37	126	178	27

caused some new errors – for instance dry shrubs below 2 m were classified as “non vegetation”. However, as dry shrubs were rare – this step still improved the overall classification accuracy. The classification accuracies were generally high and the derived classification maps represented the landscape structure and vegetation composition well (see results section).

### 2.3. Model building

#### 2.3.1. Feature preparation

We related the spectral indices derived from the Sentinel-2 satellite data to the very high resolution data from the UAS imagery. For this, we extracted the fractional cover of each of the pre- and postfire classes obtained during the supervised classification of the UAS images for each 20 × 20 m Sentinel-2 pixel overlapping with the UAS images. Further,

we extracted the mean and standard deviation of the height within each Sentinel-2 pixel using the canopy height model. We further calculated the fractional vegetation cover by first converting the canopy height model into a binary map of areas higher and lower than 1.5 m and then calculating the fractional cover of areas with a canopy height higher than 1.5 m within each Sentinel-2 pixel. The threshold of 1.5 m was selected visually and was found to adequately differentiate between open and vegetated areas while accounting for smaller inconsistencies in the canopy height model which are expected when using only UAS data for calculating canopy height. This resulted in a total of 13 features or predictor variables summarized in Table 3. After some first trial and error runs, we dropped 2 of the 13 variables due to high correlations with other variables and for other reasons specified in Table 2.

The remaining predictor variables generally showed low to moderate inter-correlations (Fig. 3).

As dependent variable, we extracted the corresponding dNBR and RdNBR values of the Sentinel-2 pixels which showed a quite high variability (Table 4). We finally filtered our feature space so that remaining S2-pixels all had a dNBR value  $\geq 0.1$  as we were mostly interested in the capabilities of dNBR to describe fire-induced changes. Values below 0.1 were assigned to unburned areas in the original categories suggested by Key & Benson (2006) as shown in Table 5. This resulted in a total of 2598 samples.

#### 2.3.2. Generalized Additive Models (GAM)

To examine the relationship between the variability of the dNBR and RdNBR indices over the study areas and the vegetation and landscape structure and composition before and after the fire, we calculated Generalized Additive Models (GAMs).

We calculated one model using all predictor variables, one model

**Table 3**

Statistical summary of the 13 features/predictor variables extracted from the UAS imagery after applying the dNBR threshold of greater than 0.1. Features not used during the modeling work-flow are in grey.

Feature	Pre- or postfire	Min	Median	Mean	Max	Rationale
%cov Pinus radiata	pre	0.0	0.40	0.41	0.91	Differences in prefire vegetation composition may have an effect on dNBR
%cov Nothofagus	pre	0.0	0.27	0.32	0.93	See %cov Pinus radiata
%cov Sclerophyll	pre	0.0	0.05	0.07	0.67	See %cov Pinus radiata
%cov dry vegetation	pre	0.0	0.0	0.01	0.50	Differences in prefire vegetation status may have an effect on dNBR
%cov non vegetation	pre	0.0	0.03	0.08	0.99	Areas not vegetated before the fire are unlikely to change
%cov shadow	pre	0.0	0.08	0.10	0.47	Correlated with Variance height and is unlikely to be a good predictor as prefire shadows also depend on view angle which is likely to differ between S2 and UAS data
%cov green vegetation	post	0.0	0.01	0.05	0.81	Green vegetation remaining after the fire should affect the dNBR due to high NIR reflection
%cov singed vegetation	post	0.0	0.03	0.11	0.77	Singed vegetation remaining after the fire should affect the dNBR due to its higher reflectance compared to charcoal
% cov non vegetation	post	0.02	0.72	0.67	1	The postfire non vegetation class represents mostly burned areas
% cov shadow	post	0.0	0.11	0.17	0.89	Shadows of standing tree trunks may influence NIR and SWIR reflectance and depend a lot on the prefire vegetation density and structure
Mean height	pre	0.0	11.60	11.58	34.52	Height metrics may serve as proxy for the amount of biomass that can be burned
Variance height	pre	0.02	13.59	18.93	149.65	See Mean height
% vegetation cover (height-based)	pre	0.0	99.64	90.57	100	Correlates with %cov non vegetation

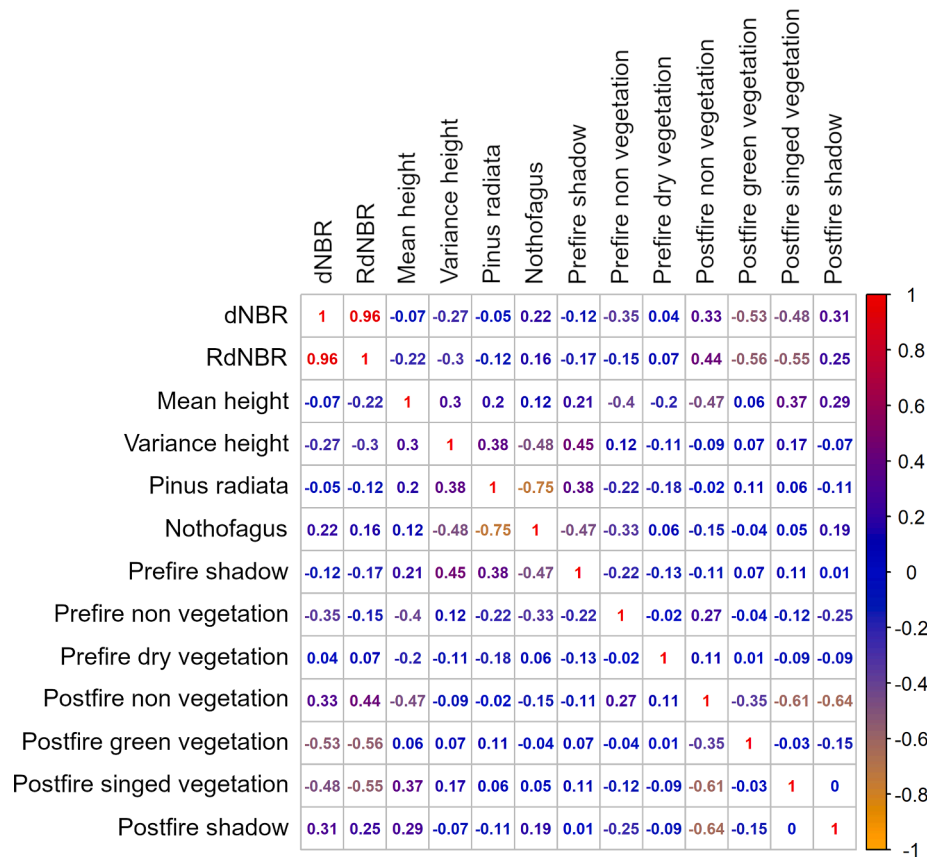


Fig. 3. Correlation plot for the two response variables (dNBR, RdNBR) and the 11 predictor variables.

**Table 4**

Statistical summary of dNBR and RdNBR values covered by the UAS flights after applying a dNBR threshold of 0.1.

Index	dNBR	RdNBR
Min	0.1	0.11
Median	0.89	1.12
Mean	0.85	1.05
Max	1.60	2.39

using only prefire variables, and one model using only postfire variables. We calculated separate models using dNBR and RdNBR as response. We additionally conducted a best-subset regression where we examined all possible combinations of predictors for models with 2–10 predictor variables and identified the best models using lowest Akaike Information Criterion (AIC) as indicator.

We applied the GAM algorithm implemented in the R-package “mgcv” (Wood, 2011) using the “REML” (restricted maximum likelihood) automatic smoothing parameter option. We also activated the internal variable selection to identify unnecessary predictor variables.

**Table 5**  
 Categorization of severity classes based on dNBR values as suggested by Key & Benson (2006).

Severity level	dNBR range
Enhanced regrowth (high)	-0.5 to -0.251
Enhanced regrowth (low)	-0.25 to -0.101
Unburned	-0.1 to 0.099
Low severity	0.1 to 0.269
Moderate-low severity	0.27 to 0.439
Moderate-high severity	0.44 to 0.659
High severity	0.66 to 1.3

As we were not interested in the predictive performance of the models, but rather in explaining the relation between the response and the predictor variables, we report detailed model results for models using all available samples during the model building. However, we provide additional model performances based on cross-validated models with repeated data splits where we always used 70% of the samples for training and 30% for validation.

### 3. Results

#### 3.1. Supervised classification of UAS flights

The overall accuracies for the supervised classifications of all six UAS datasets obtained from the five-fold cross-validation range between 86.3% and 90.6% for the prefire classification and 90.1% and 95.1% for the postfire classifications (Table 6).

#### 3.2. Best subset selection GAM

The best subset selection results indicate that best models with 5 to 10 predictors show hardly any difference in model performances when compared to the model using all predictors (Fig. 4) (differences of 0.008 and 0.013 in adjusted  $R^2$  for dNBR and RdNBR, respectively – see also Fig. 5). Models with 2–4 predictors show larger performance losses (up to 0.209 and 0.101 difference in adjusted  $R^2$  for dNBR and RdNBR, respectively).

The variables selected in the two first ranked best subset models with 2–10 predictor variables and for the response variables dNBR and RdNBR are summarized in Table 7 and 8, respectively. Postfire variables (grey rows in Table 7 and 8) were generally more represented in sparse models than prefire variables. Vegetation type specific predictor variables were only selected in models with 5 and more predictors with “Cover of Sclerophyll forest” being the most frequently selected class. Most frequently selected prefire predictor is “prefire non vegetation”. Accuracies, similar to the reference model using all predictor variables were obtained when combining a set of 2–3 postfire variables with the “prefire non vegetation” and the “mean height” variables. These results are very similar for models using dNBR and RdNBR as response. In case of dNBR, most second ranked models show similar AIC values as the best subset model (Supplementary Material 2). In case of RdNBR, the performances of the second ranked models deviate more, particularly for models with 2–4 predictor ranked variables (Supplementary Material 2).

**Table 6**  
 Overall accuracies of the supervised SVM classifications of the UAS flights.

Index	Prefire	Postfire
Site 1	90.0	91.2
Site 2	86.3	92.6
Site 3	88.2	94.3
Site 4	86.7	90.1
Site 5	90.6	95.1
Site 6	87.7	94.3

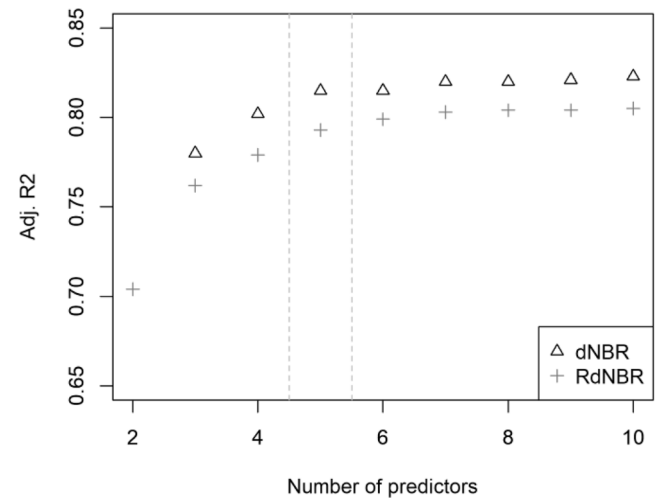


**Fig. 4.** Best subset selection results. Adjusted  $R^2$ -values of the best Generalized Additive Model models selected during the best subset selection are plotted over the number of predictors. Best model for each number of predictors was selected according to minimum Akaike Information Criterion (AIC). The models with 5 predictors are marked with the two vertical grey lines and will be discussed with more details below.

#### 3.3. Detailed GAM results

GAM models based on all predictor variables performed best, for both dNBR and RdNBR (approximately 82% and 75% explained variability) (Fig. 5). Postfire predictors alone were able to explain about 70% of the variability in dNBR and RdNBR. Using only prefire predictors led to notably reduced abilities of the models to explain the variability in dNBR and RdNBR values (explained variance of approximately 37% and 29%, respectively). Overall, the median adjusted  $R^2$  values from models applying repeated data-splits resulted in lower accuracy than the models using all samples during model training. The drops in accuracy when applying repeated data-splits were higher for RdNBR than for dNBR. For the latter, in most cases, the accuracies reported for the models using all samples were within the range of values observed for the iterative validation. The two best subset selection models with 5 predictors showed similar performances as the models using all predictor variables. Best very sparse models based on only two predictor variables still explain about 60% of the variance in dNBR and RdNBR values.

The corresponding scatterplots confirm the reported numerical correlation trends and show very high correlations between predicted and observed dNBR values for models using all predictor variables and the 5 predictor model of the best subset regression (Fig. 6). The scatterplots for RdNBR are very similar to the results for dNBR and are only presented in the Appendix (Supplementary material 3).

In the following, we will have a closer look at the best subset model with 5 predictor variables (representing a parsimonious model which performs nearly equally well as the reference model with all predictors) and additionally at the two models with only 2 predictor variables, which still show a comparably high ability to explain the variance of dNBR values. We focus on these models as they are more suitable for interpretation than the models with more predictors.

#### 3.4. Response curves

Response curves of GAM models indicate the relation between an individual predictor and the response variable, taking into account the influence of the other predictor variables in the GAM. In the best subset regression model with 5 predictors, the variables “prefire non vegetation”, “postfire green vegetation” as well as “postfire singed vegetation” show a negative relation with dNBR values with increasing coverage

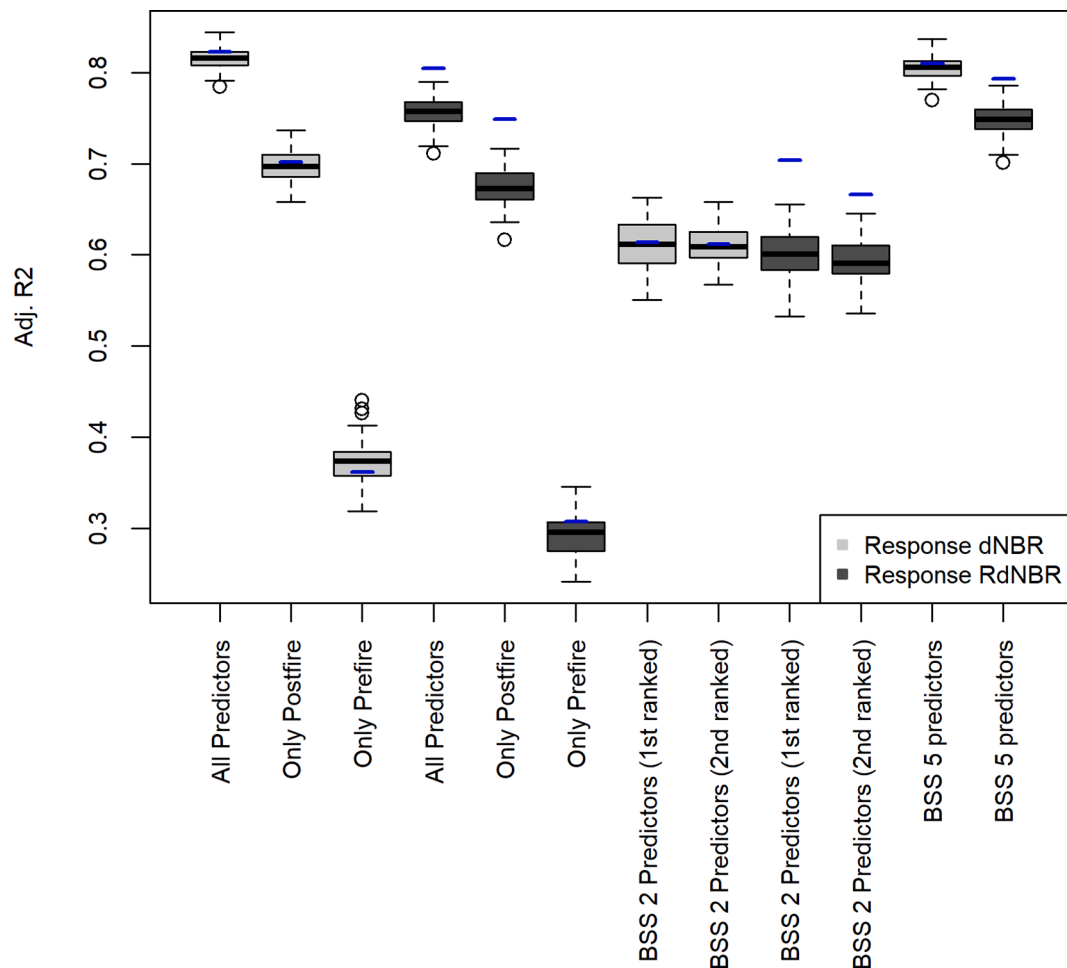


**Fig. 5.** Iterative adjusted  $R^2$  values of GAM models using all, only postfire and only prefire predictors and using dNBR and RdNBR as response variable. The same results are presented for the two first ranked best subset (BSS) regression models using two and the first ranked model using five predictor variables. Boxplots indicate  $R^2$  value ranges of 100 iterative model runs splitting the available data into 70% training and 30% validation samples. Blue horizontal lines indicate corresponding performances of models trained with all samples. (For interpretation of the references to colour in this figure legend, the reader is referred to the web version of this article.)

**Table 7**

Selected predictors of the two best performing models with 2–10 predictor variables and dNBR as response. A + indicates that the predictor was selected once in the two models, ++ indicates that the predictor was selected in both models. Grey + indicates a selection in the second best model. Grey rows in the table mark postfire predictors.

No. of variables	2	3	4	5	6	7	8	9	10
<b>Variable</b>									
Mean height				+	++	++	++	++	++
Variance height					+	+	++	+	++
Pinus radiata [%]								++	+
Nothofagus [%]						+		++	++
Sclerophyll [%]				+	+	++	++	++	++
Prefire non vegetation [%]		++	++	++	++	++	++	++	++
Prefire dry vegetation [%]							+		+
Postfire non vegetation [%]	+	+	+	++	++	++	++	++	++
Postfire green vegetation [%]	+	+	++	++	++	++	++	++	++
Postfire singed vegetation [%]	+	+	++	++	++	++	++	++	++
Postfire shadow [%]	+	+	+				+	+	++

(Fig. 7). The trends of the additional two variables “mean height” and “postfire non vegetation” are less clear and the curves fluctuate around dNBR values of 0 which suggests a smaller influence of these two predictors. The “postfire non vegetation” variable shows overall a small negative trend, while the mean height variable first shows a slight positive trends with dNBR for heights between 0 and 5 m, then a

negative trend between 5 and approximately 12 m before the curve levels off at a value of close to 0.

The first ranked best subset regression model with two predictors consists of the two predictor variables “postfire green vegetation” and “postfire singed vegetation” which were both also included in the best model with five predictor variables (Fig. 8). Both variables show a more

**Table 8**

Selected predictors of the two best performing models with 2–10 predictor variables and RdNBR as response. A + indicates that the predictor was selected once in the two models, ++ indicates that the predictor was selected in both models. Grey + indicates a selection in the second best model. Grey rows in the table mark postfire predictors.

No. of variables	2	3	4	5	6	7	8	9	10
<b>Variable</b>									
Mean height				+	++	++	++	++	++
Variance height					+	+	++	++	++
Pinus radiata [%]								+	+
Nothofagus [%]						+		++	++
Sclerophyll [%]				+	+	++	++	++	++
Prefire non vegetation [%]		++	++	++	++	++	++	++	++
Prefire dry vegetation [%]							+		+
Postfire non vegetation [%]	+	+	+	++	++	++	++	++	++
Postfire green vegetation [%]	+	+	++	++	++	++	++	++	++
Postfire singed vegetation [%]	+	+	++	++	++	++	++	++	++
Postfire shadow [%]	+	+	+				+	+	++

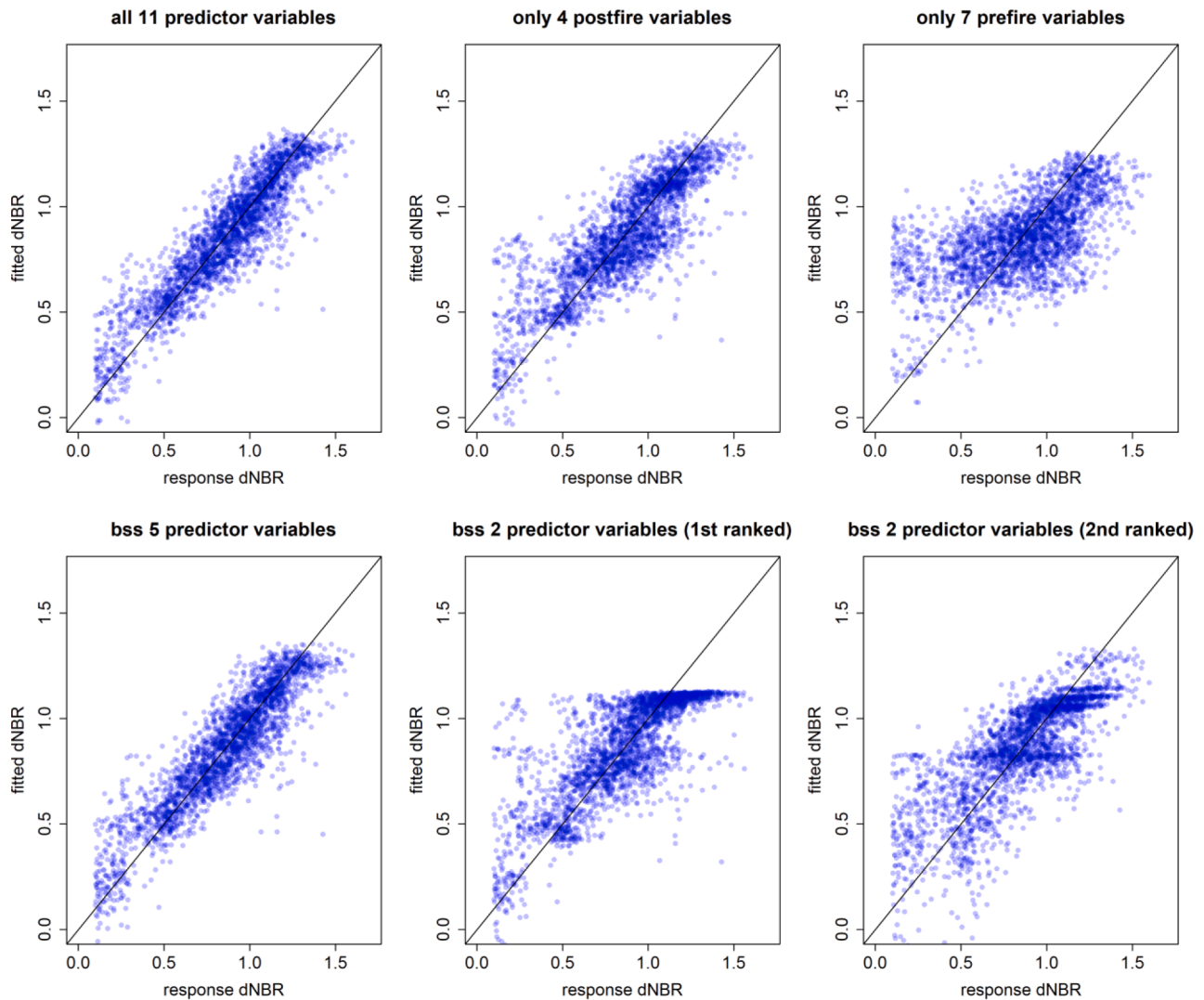


**Fig. 6.** Scatterplots corresponding to the same models presented in Fig. 5 and trained with all available samples, using dNBR as response.

or less clear negative trend with dNBR and hence a similar behavior as in the model with five predictors.

The second ranked best subset regression model with two predictors includes the variables “postfire non vegetation” and “postfire shadow” (Fig. 9). In this model both variables show a clear positive trend with dNBR which suggests that an increased cover of “postfire non

vegetation” and “postfire shadows” leads to higher dNBR values if only these two variables are considered.

The response curves for RdNBR closely followed the results for the dNBR models and are only presented in the [Supplementary Material \(Supplementary material 4\)](#). Response curves for all other models are also included there ([Supplementary Material 4](#)).

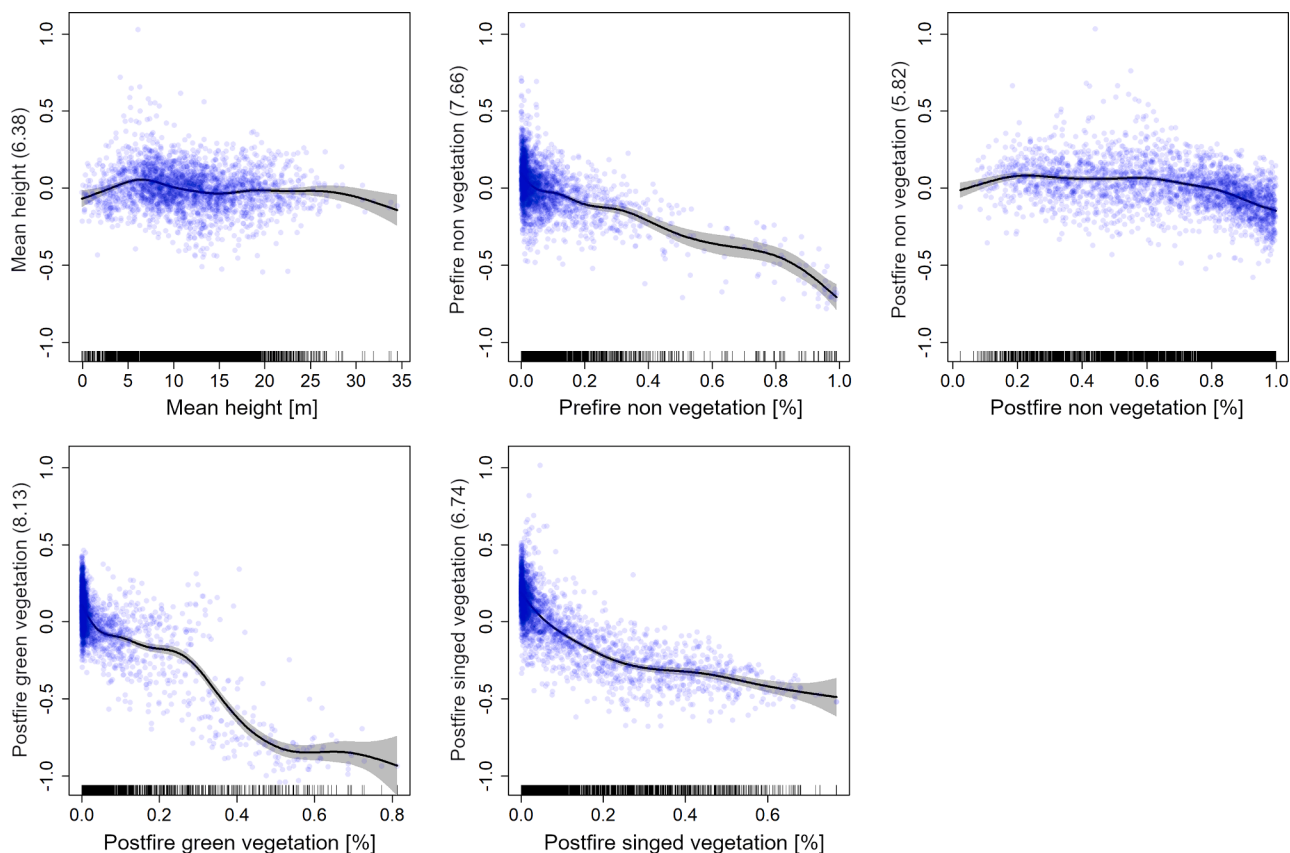


Fig. 7. Response curves for the best subset selection model with five predictors and using dNBR as response variable. Units on x-axes are fractional cover values (1 = 100%) for all predictors except for mean height which is in meters [m].

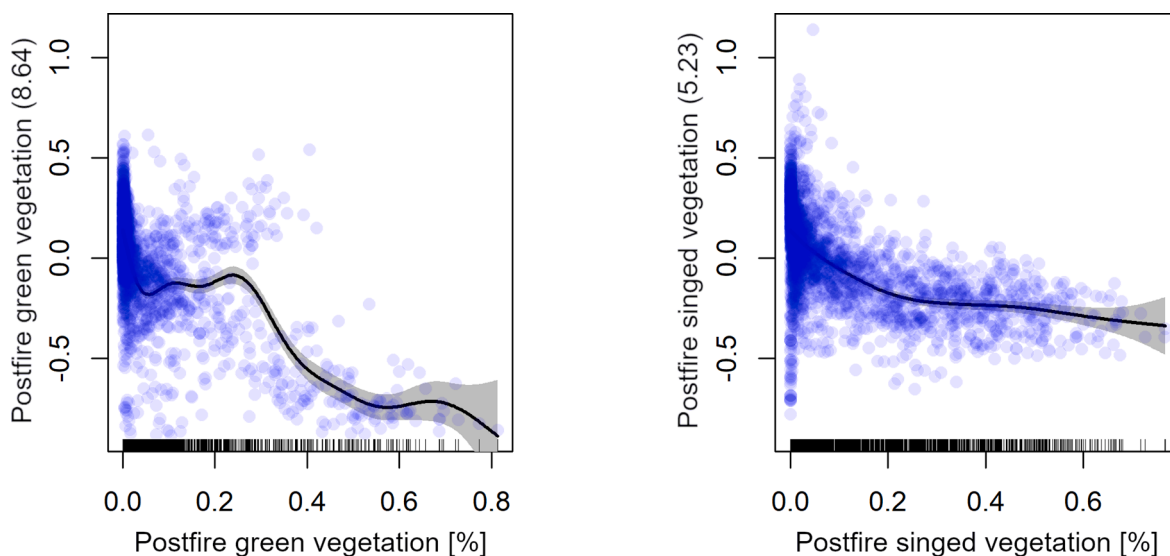


Fig. 8. Response Curves for the best subset selection model with 2 predictors and using dNBR as response variable. Units on x-axes are fractional cover values (1 = 100%).

### 3.5. Maps

Besides the numerical results, we present maps of four subsets of the study area for additional context and for better understanding the modeling results. The first map shows a subset of test site 1, which displays a completely burned area (Fig. 10). The prefire vegetation was dominated by the “Sclerophyll” and “Pinus radiata” classes while no

living vegetation is apparent in the postfire UAS images. In the corresponding classification maps, we can see that some areas that appear to be a mix of burned organic material and shadows were misclassified as green vegetation. This problem was only observed for this UAS scene and explains the small bump in the response curve of “postfire green vegetation” at fractional covers of 0.2–0.25 (Figs. 7 and 8). Concerning the dNBR and RdNBR maps, we can observe a local maximum in the

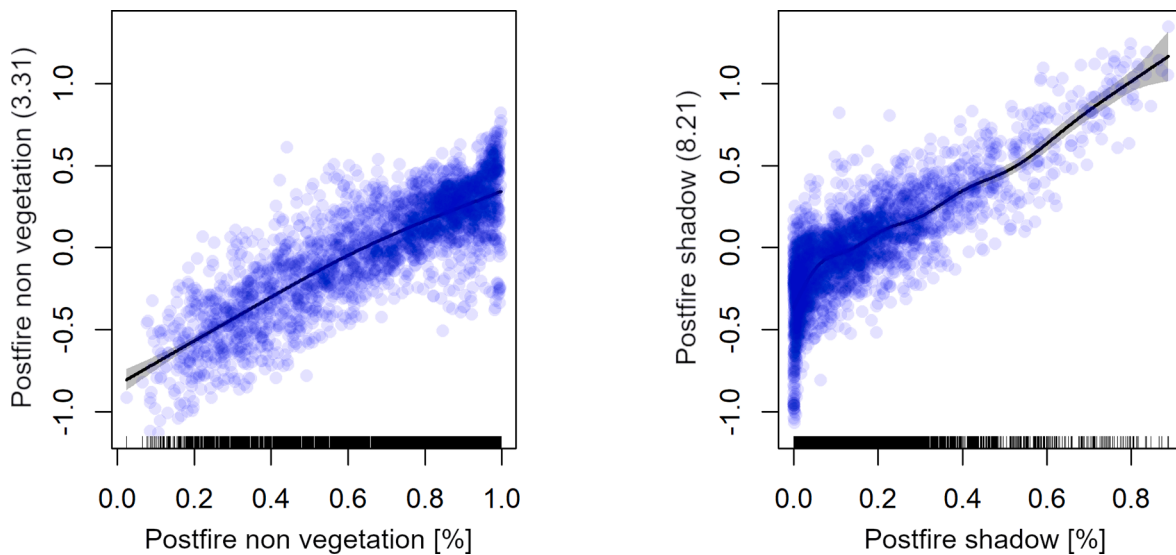


Fig. 9. Response Curves for the second best subset selection model with two predictors and using dNBR as response variable. Units on x-axes are fractional cover values (1 = 100%)

eastern part of the image. This maximum seems to be particularly related to an area which appears very dark in the postfire UAS image and which was assigned to the shadow-class in the postfire UAS classification. The visual appearance confirms that there are a lot of shadows in this area. The shadows seem to partly relate to standing snags and partly to terrain shadows. The prefire UAS image does not show a particularly high vegetation cover in this area (at least there are other areas with similar cover). Hence, the shadow seems to play an important role for causing the dNBR maximum. Further, a slight gradient of dNBR and RdNBR values can be observed from the local maximum in the East towards the western edge of the area. According to the prefire UAS image, this may relate to a canopy cover density gradient with lower canopy cover in the western parts of the depicted area. In these areas higher coverages of the “prefire non vegetation” class can be observed and these spatially match well with lower dNBR and RdNBR values.

The second map shows a subset of test site 4 which was dominated by a mix of *Nothofagus* and *Sclerophyll* forests before the fire. Some intermixed *Pinus radiata* individuals occur as well (Fig. 11). The canopy coverage was high throughout the area and some smaller patches of dry vegetation are visible in the north-western parts of the scene. After the fire, most of the vegetation is burned completely, but some smaller forest areas with singed leaves remained. The singed areas show lower dNBR and RdNBR values which is in line with the response curve of “postfire singed vegetation” (Fig. 8). Similarly, as in the first map, a local maximum with particularly high RdNBR and dNBR values exists in the center north of the area. Again, we can observe particularly dark areas in the postfire UAS image which again suggests a notable influence of shadow and maybe also an accumulation of charcoal in these areas (even though we did not note such accumulations in the field during the UAS campaigns). Interestingly, the areas with particularly high RdNBR and dNBR values show mostly dead trees which still maintain their coarse crown structures. In other parts of the scene, where only snags remained after the fire (for example at the bottom of the eastern edge of the scene), the RdNBR and dNBR values tend to be lower.

The third map shows another subset of test site 4 which was dominated by *Sclerophyll* and *Nothofagus* forests before the fire and burned completely (Fig. 12). The postfire UAS image shows a distinct pattern of three linear dark features expanding in North-South direction with a slight shift. These patterns also appear in the corresponding dNBR and RdNBR maps. We assume that these features correspond to small creeks which tend to have vertically denser and more diverse vegetation layers due to the favorable hydric conditions and the protections against

winds. The first impression is that the dark appearance of these areas are exclusively driven by topographic shadows. However, a closer look suggests, that, similarly as for the second map, the areas are also densely stocked with standing dead trees with intact crown structures which may also contribute to the observed strong shadows.

Finally, the fourth map shows a subset of test site 5 which was covered by a mix of *Sclerophyll* and *Pinus radiata* forests before the fire (Fig. 13). This site burned only partly and after the fire a notable fraction of green vegetation remained in the southern parts of the area while singed vegetation can be found in most parts of the scenes. Only about 30% of the area burned completely. The gradient from remaining green vegetation to singed vegetation and completely burned areas is nicely mirrored in the dNBR and RdNBR maps which show low, intermediate and high values for the three classes, respectively.

#### 4. Discussion

Here, we applied very high resolution UAS imagery collected briefly before and after a large wildfire in Chile to derive information about the landcover and vegetation composition before and after the fire and used this information to explain dNBR and RdNBR variability as captured by two Sentinel-2 scenes. As our postfire imagery was collected shortly after the wildfires, we assume that the majority of (R)dNBR variability induced by the fire relates to fire severity according to the definition of Lentile et al. (2006). However, as no detailed ecological field data were available, we avoid discussing fire and burn severity differences in this study.

With the UAS approach we provide a new perspective that complements the findings of earlier studies who examined dNBR variability using pre- and postfire vegetation structure obtained from LiDAR data (e.g., McCarley et al., 2017; Viedma et al., 2020; Wulder et al., 2009) or from field surveys (e.g., Harvey et al., 2019). In the following we will first discuss the UAS classifications which led to our explanatory variables, then we will reflect on the obtained model performances and interpret the results concerning how the considered landcover classes drive the dNBR and RdNBR signal. We will conclude with some thoughts about the limitations of this study.

##### 4.1. Extraction of vegetation variables from UAS data

The classification of the pre- and postfire UAS images into 6 and 4 landcover classes, respectively, resulted in high overall accuracies

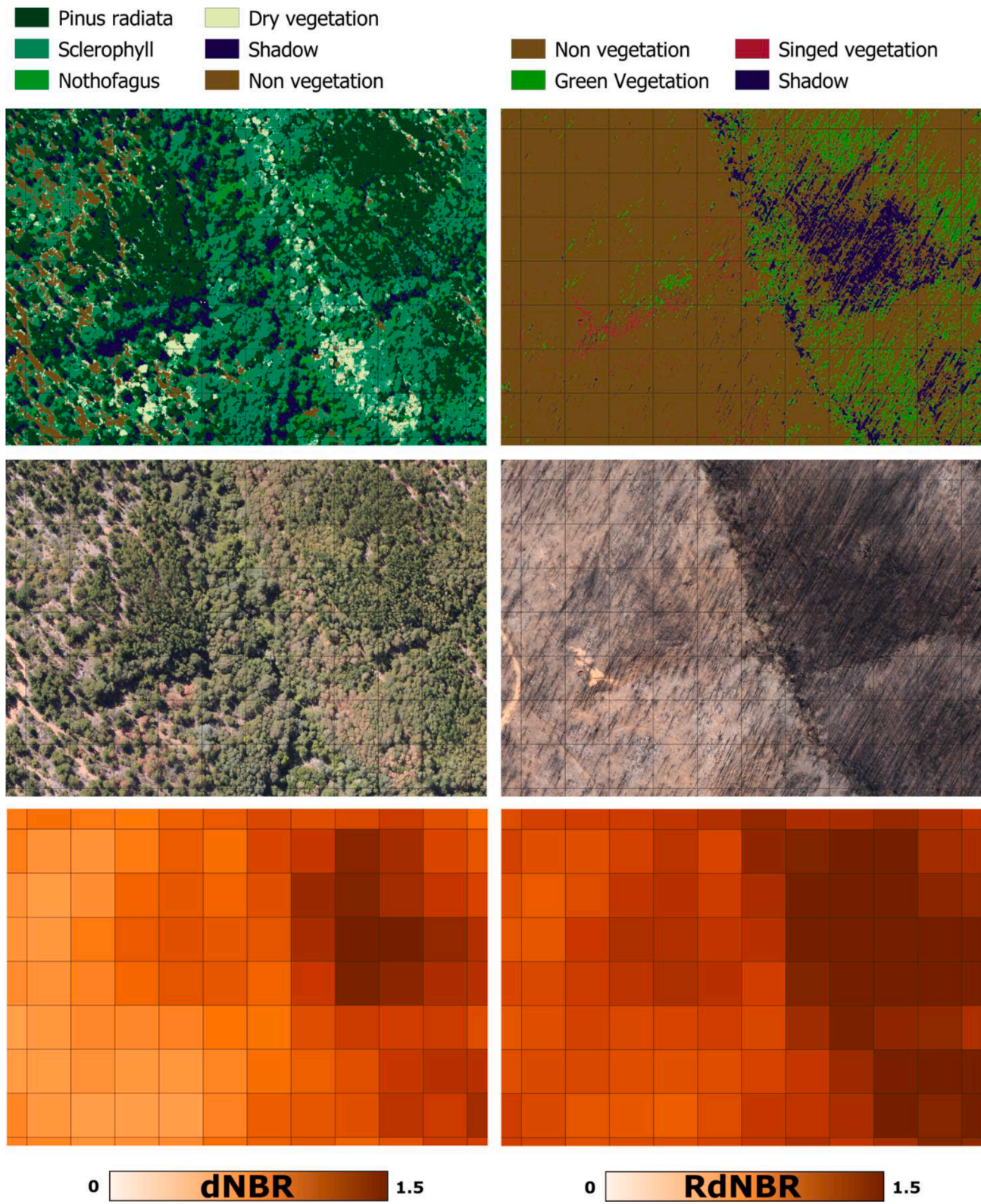


Fig. 10. Subset of test site 1, showing pre- and postfire classification maps (top row), pre- and postfire UAS images (middle row) and Sentinel-2 based RdNBR and dNBR images (bottom row). Center coordinate of the scene is E: 745840 N: 6,071,099 (coordinate reference system: WGS 84, UTM 18S, EPSG: 32718). The depicted grid has a size of 20 × 20 m. North is up.

(86.3%-94.3%). The corresponding classification maps are depicting the visual impression of the landscape composition well (see Figs. 10–13). An exception to the overall good results is the “postfire green vegetation” class in test site 1, which was overpredicted quite notably (Fig. 10).

We explain this with a general scarcity of green vegetation in this postfire scene, which has hampered the collection of an adequate training dataset for this class. As only one of the six postfire UAS scenes was affected by this problem, we consider this problem to be negligible

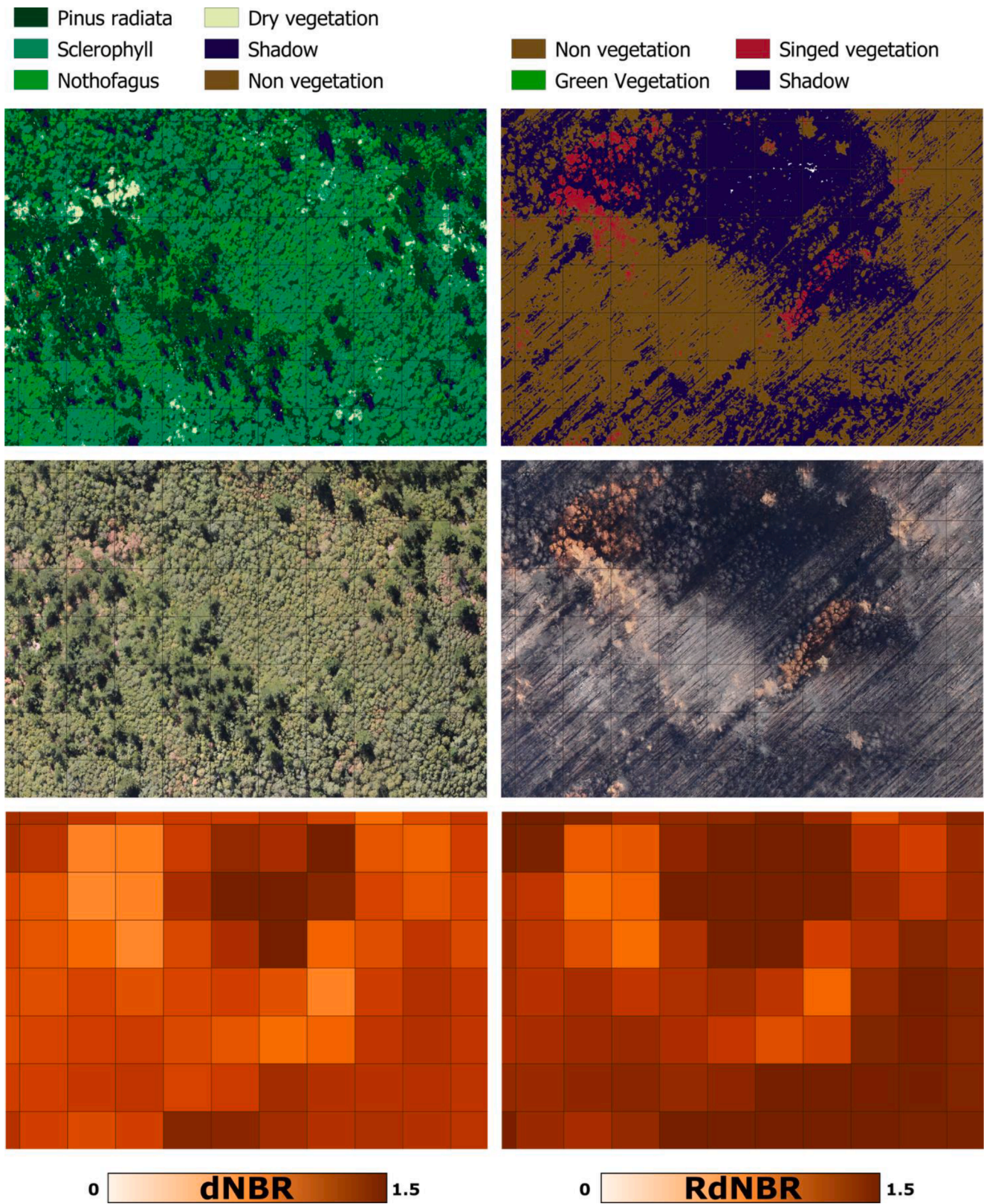
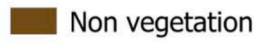
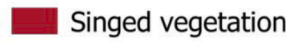
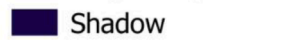
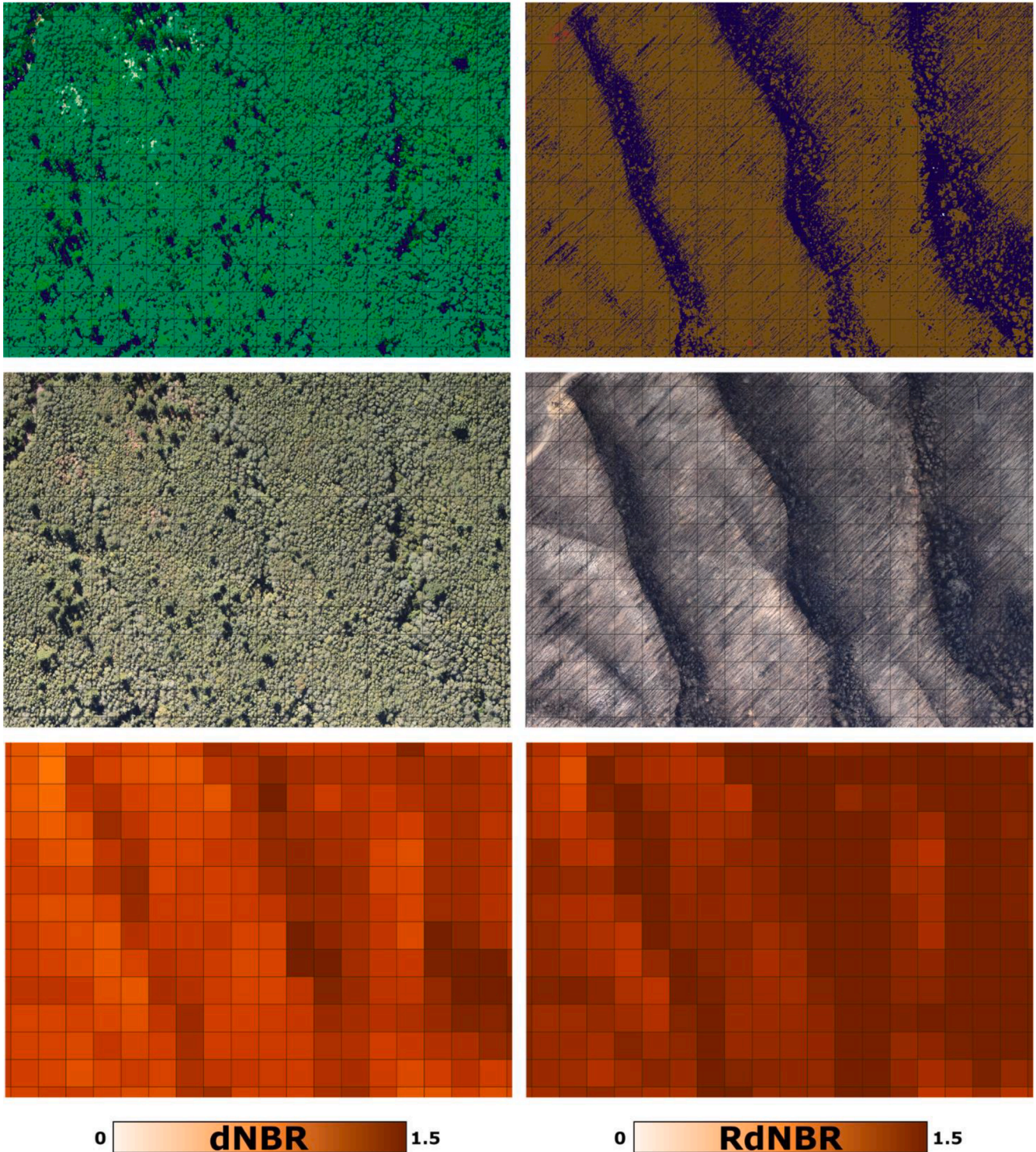


Fig. 11. First subset of test site 4, showing pre- and postfire classification maps (top row), pre- and postfire UAS images (middle row) and Sentinel-2 based RdNBR and dNBR images (bottom row). Center coordinate of the scene is E: 749014 N: 6,079,150 (coordinate reference system: WGS 84, UTM 18S, EPSG: 32718). The depicted grid has a size of 20 × 20 m. North is up.

 Pinus radiata	 Dry vegetation
 Sclerophyll	 Shadow
 Nothofagus	 Non vegetation

 Non vegetation	 Singed vegetation
 Green Vegetation	 Shadow



**Fig. 12.** Second subset of test site 4, showing pre- and postfire classification maps (top row), pre- and postfire UAS images (middle row) and Sentinel-2 based RdNBR and dNBR images (bottom row). Center coordinate of the scene is E: 749311 N: 6,079,017 (coordinate reference system: WGS 84, UTM 18S, EPSG: 32718). The depicted grid has a size of 20 × 20 m. North is up.

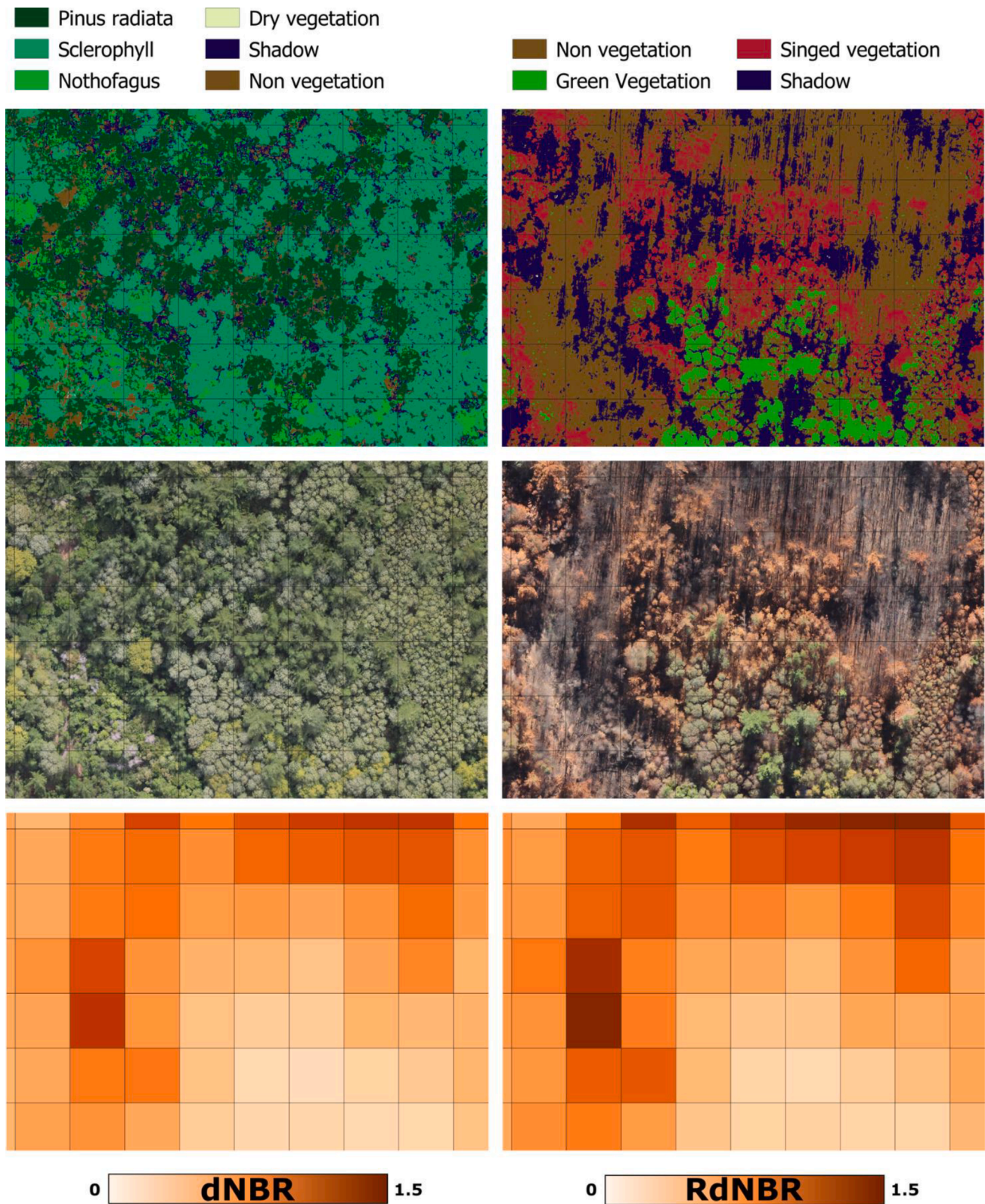


**Fig. 13.** Subset of test site 5, showing pre- and postfire classification maps (top row), pre- and postfire UAS images (middle row) and Sentinel-2 based RdNBR and dNBR images (bottom row). Center coordinate of the scene is E: 760646 N: 6093841 (coordinate reference system: WGS 84, UTM 18S, EPSG: 32718). The depicted grid has a size of 20 × 20 m. North is up.

even though it is likely that the small bump in the otherwise clearly declining response curve of the “postfire green vegetation” class (Figs. 7 and 8) originates from these misclassifications. We restricted the number of landcover classes to 6 and 4 classes in the pre- and postfire UAS

images, as these classes were clearly separable via visual interpretation and we considered them to have a relevant influence on the dNBR signal. If higher spectral resolution UAS images and corresponding reference data from the field would be available, a discrimination of more classes,

particularly for the postfire situation, could be beneficial for a deeper understanding of the dNBR signal. Such classes could for example include standing dead wood and rocks (see also discussion about shadows below).

In our study we followed a pixel-based approach to classify the UAS images into the considered landcover classes. Recently emerging deep learning algorithms may be able to further improve UAS-based vegetation classifications where the spectral information is limited but detailed textural information is available due to the very high spatial resolution of the UAS data (e.g., Ferreira et al., 2020; Hamylton et al., 2020; Kattenborn et al., 2020; Torres et al., 2020). As these deep learning algorithms require a notably larger amount of training data and our classification results were generally satisfying, we did not pursue such an approach in our study.

Instead of classifying the UAS images into discrete landcover classes, it is also possible to extract a continuous greenness signal from the UAS images as proxy for the prefire vegetation composition. We examined this approach as well but did not find good correlations between the variability in greenness in the UAS and the Sentinel-2 based dNBR and RdNBR variability (results not shown). It can be assumed that the radiometric variability between the individual UAS flights (taken under different acquisition conditions) and the generally restricted radiometric resolution of the applied consumer camera hamper this approach. Radiometric calibration procedures for UAS systems are available (e.g., Guo et al., 2019) but the required field data from calibration targets were not available for our dataset. Even with an appropriate radiometric calibration the relation between the greenness signal and dNBR may still be limited as the dNBR bases on information from the NIR and SWIR region and not the visual part of the spectrum.

#### 4.2. Which variables explain the variability in dNBR?

GAM models trained with all UAS-based landcover classes were able to explain more than 80% of the variance of Sentinel-2 based dNBR values and more than 75% of the variance in RdNBR (Fig. 5). Models trained with only postfire predictors performed notably better than models trained with only prefire predictors. On the other hand, prefire predictors are still able to explain around 35% and 30% of the variance in dNBR and RdNBR, respectively. This suggests that the prefire landscape composition, and presumably particularly the prefire vegetation cover, which was found to be the most important prefire predictor, has a notable influence on the resulting (R)dNBR index values. The fact that prefire predictors perform slightly better for explaining dNBR values than for RdNBR values does not necessarily confirm the ability of the RdNBR to account for prefire vegetation composition, as RdNBR models were generally found to perform slightly weaker than dNBR models (Fig. 5). Viedma et al., (2020) also reported that variables related to vegetation structure better explained variability in dNBR than in RdNBR. However, the authors related this mostly to outlier values in their RdNBR dataset which were not occurring in our study.

Interestingly, models trained with all 11 landcover classes performed merely better than models with only 5 predictor variables which were identified during the best subset analysis. This indicates that most of the variability in the NBR indices can be explained with a parsimonious set of land-cover class fractions. According to our results, the most important land-cover classes selected for the parsimonious models with 2–5 predictors are “prefire non vegetation”, “postfire non vegetation”, “postfire green vegetation” and “postfire singed vegetation”. All of these classes relate to the overall amount of burned vegetation surface which seems to be the key driver of Sentinel-2 based dNBR and RdNBR variability in the examined landscape. This somewhat confirms earlier studies based on pre- and postfire LiDAR data which identified the variables “change in crown closure” (Wulder et al. 2009) and “change in canopy cover” (McCarley et al. 2017) to be amongst the most important variables for explaining the variability of dNBR-like indices.

Height information was found to be of moderate importance and was

included in models with 5 or more predictors. The response curve of the “mean height” predictor showed no clear trend with dNBR or RdNBR (Fig. 7). A visual comparison between the patterns of canopy height and the resulting dNBR and RdNBR values confirmed that there are no clear patterns apparent (results not shown). Canopy height is known to be a good proxy for vegetation biomass (e.g., Tonolli et al., 2011). The fact that it hardly relates to variability in dNBR and RdNBR again confirms that in the examined landscape, (R)dNBR is rather a proxy for burned vegetation cover than for burned vegetation mass.

Prefire vegetation type composition played only a marginal role in explaining the variability in dNBR and RdNBR in our study and the corresponding predictors were only selected in models with higher number of predictors. This may relate to the generally high intensity of the fire in our test site, which burned as crown fires across most areas leading to high levels of combustion of all available vegetation, independent from its structure and species composition. A small exception were riparian vegetation areas which were on average less affected by the fire; but these areas did not cover notable parts of our test sites. In fires with overall lower intensities, vegetation types may relate notably stronger to the amount of canopy cover consumed and hence the observed fire or burn severity. For example Viedma et al., (2020) identified vegetation composition and biomass to be a very important driver of fire severity in a mixed-severity fire in Spain. Here, the vegetation types were in many cases decisive whether the fire burned more or less intensively and the corresponding patterns also emerged in the NBR-based indices.

Aside the best performing GAM models, we also presented two models based on only two postfire predictor variables which were able to explain about 60% of the variability in (R)dNBR values. The first ranked model selected “postfire green vegetation” and “postfire singed vegetation” as predictor variables. This is in line with the results for the model based on 5 predictors and again confirms that most of the variability in the dNBR indices apparently relates to the consumption or survival of green vegetation cover. On the other hand, the second ranked model selected “postfire non vegetation” and “postfire shadow” as most important variables. Both, the “postfire non vegetation” and the “postfire shadow” class show a positive, linear relation to dNBR values. While this is expected for the “postfire non vegetation” class which represents mostly burned areas, the interpretation of this outcome for the “postfire shadow” class is less straightforward. The spatial patterns of the shadow class in Figs. 10–13 suggest that areas classified as shadows mostly occur in areas with a high density of snags of dead trees and in areas with dead standing trees with remaining crown structures and in areas influenced by terrain shadows (Fig. 13). In Fig. 11, an area appearing very dark in the postfire UAS image coincides with a local maximum in dNBR values. The UAS image shows a comparably high fraction of standing dead trees with remaining crown structures in this area which cast a comparably high amount of shadows contributing to the dark appearance of the area. On the other hand, areas with similar vegetation densities before the fire but a complete combustion of the crowns (and only snags remaining) appear notably brighter in the postfire UAS image and also typically show lower dNBR values. This may suggest that shadows shed by standing leafless dead trees with intact crown structures may have a quite notable, potentially misleading, influence on the observed dNBR values. The gravity of this effect is likely to vary with solar elevation angle during the satellite data acquisition. Additionally it has to be considered that the slope and aspect of the terrain determines the projection and, thereby, total cover of cast shadows on the ground (Kattenborn et al., 2018), which in turn may introduce substantial local variability in dNBR values.

The problematic influence of shadows on dNBR values has earlier been discussed by Hoy et al., (2008), who also specifically addressed variation in solar elevation angles and topography. Both were found to notably affect the remote sensing signal of forest stands (Verbyla et al., 2008). However, the potential influence of shadows cast by remaining standing woody vegetation after a fire has not been extensively

discussed yet. One reason for this might be the fact that in medium resolution optical data that is often used for dNBR analysis (e.g. Landsat or Sentinel-2), cast shadows are not directly identifiable and their influence on NBR-related products could be mistaken as a signal of accumulated charcoal on the ground as both phenomena lead to a general drop in reflectance. [Chuvienco et al., \(2007\)](#) mentioned cast shadows as an issue when they attempted to simulate the signal of burned vegetation areas using a radiative transfer model that assumed horizontally homogeneous vegetation layers. The model failed to accurately simulate the reflectance signal of the burned areas of the examined heterogeneous landscape in which cast shadows were present and which hence deviated notable from the assumption of a horizontally homogeneous vegetation canopy.

#### 4.3. Limitations and considerations

The most severe limitation of our study is that we have no detailed field data available. As a consequence, some of our defined land-cover classes are defined rather widely (e.g., the “postfire non vegetation” class). Detailed information from the field may have helped to differentiate the UAS information into more classes and hence enable a more detailed thematic analysis of dNBR variability. On the other hand, our dataset is unique in that it provides detailed, fine-grained and spatially continuous information about the landscape composition before and after the wildfire. Such UAS data overcome some typical limitations of field sampling surveys after wildfires which are often at least partly constrained by accessibility and limited sampling frequency and lack spatial continuity. The latter makes it often challenging to collect representative field data matching the spatial resolution of the satellite sensor and the environmental variability (e.g., [Hoy et al., 2008](#)). The potential of UAS data to partly replace field reference data in situations where the target classes can be clearly identified by visual interpretation has also recently been discussed with more detail in [Kattenborn et al. \(2019b, 2020\)](#), who also mention that the shared bird’s eye perspective of UAS and satellite data is a big advantage. This shared perspective proved to be particularly interesting for effectively analyzing the influence of cast shadows.

A further limitation of our study is that our findings are restricted to a single wildfire event in central Chile. This particular fire was one of the most severe fires that has ever occurred in central Chile since fires are recorded and may hence not be a representative example for an average wildfire in Chile let alone a Mediterranean landscape. Nevertheless, our findings may be the starting point for further investigations with comparable datasets. The increasing number of UAS surveys for ecological applications constantly increases the chances to coincidentally capture landscapes briefly before a wildfire event. If a recently surveyed area is affected by a wildfire, a follow-up UAS campaign may often be organized with limited efforts. In ideal case, these postfire UAS campaigns should be accompanied by a field survey collecting further ecological information that subsequently can be upscaled with the UAS data and then used to explain fire severity patterns observed by satellites. It may also be possible to conduct a corresponding investigation in the context of prescribed burnings or even a controlled wildfire experiment.

#### 5. Conclusions

We derived pre- and postfire landscape composition from UAS imagery acquired briefly before and after a wildfire in central Chile. We used several vegetation-related variables derived from the UAS imagery to explain dNBR and RdNBR variability captured by Sentinel-2 satellite data. Our results suggest that: (i) in our study area the largest fraction of variability in Sentinel-2 based dNBR and RdNBR values can be explained by the fraction of consumed canopy cover (ii) vegetation composition before the fire did not have a large influence on dNBR and RdNBR variability (iii) cast-shadows of snags and standing dead trees with remaining crown structure may have a notable influence on the dNBR

signal.

#### CRediT authorship contribution statement

**Fabian Ewald Fassnacht:** Conceptualization, Methodology, Software, Formal analysis, Investigation, Writing - original draft, Visualization, Resources, Funding acquisition. **Ephraim Schmidt-Riese:** Conceptualization, Methodology, Software, Formal analysis, Investigation, Visualization, Writing - review & editing. **Teja Kattenborn:** Conceptualization, Methodology, Writing - review & editing. **Jaime Hernández:** Resources, Funding acquisition, Writing - review & editing.

#### Declaration of Competing Interest

The authors declare that they have no known competing financial interests or personal relationships that could have appeared to influence the work reported in this paper.

#### Acknowledgements

This study was conducted within the SaMovar project (Satellite-based Monitoring of invasive species in central Chile) at the Karlsruhe Institute of Technology and the Technical University of Berlin. The project is funded by the German National Space Agency DLR (Deutsches Zentrum für Luft- und Raumfahrt e.V.) on behalf of the German Federal Ministry of Economy and Technology based on the Bundestag resolution 50EE1535 and 50EE1536. We furthermore acknowledge the European Union and ESA for providing free Copernicus data. We acknowledge support by the KIT-Publication Fund of the Karlsruhe Institute of Technology.

#### Appendix A. Supplementary data

Supplementary data to this article can be found online at <https://doi.org/10.1016/j.jag.2020.102262>.

#### References

- Alonso-Canas, I., Chuvienco, E., 2015. Global burned area mapping from ENVISAT-MERIS and MODIS active fire data. *Remote Sens. Environ.* 163, 140–152. <https://doi.org/10.1016/j.rse.2015.03.011>.
- Attwill, P.M., 1994. Ecological disturbance and the conservative management of eucalypt forests in Australia. *For. Ecol. Manage.* 63 (2–3), 301–346. [https://doi.org/10.1016/0378-1127\(94\)90115-5](https://doi.org/10.1016/0378-1127(94)90115-5).
- Balch, J.K., Bradley, B.A., Abatzoglou, J.T., Chelsea Nagy, R., Fusco, E.J., Mahood, A.L., 2017. Human-started wildfires expand the fire niche across the United States. *PNAS* 114 (11), 2946–2951. <https://doi.org/10.1073/pnas.1617394114>.
- Bourgeau-Chavez, L.L., Harrell, P.A., Kasischke, E.S., French, N.H.F., 1997. The detection and mapping of alaskan wildfires using a spaceborne imaging radar system. *Int. J. Remote Sens.* 18 (2), 355–373. <https://doi.org/10.1080/014311697219114>.
- Cansler, C.A., McKenzie, D., 2012. How robust are burn severity indices when applied in a new region? Evaluation of alternate field-based and remote-sensing methods. *Remote Sens.* 4 (2), 456–483. <https://doi.org/10.3390/rs4020456>.
- Chuvienco, E., DeSantis, A., Riaño, D., Halligan, K., 2007. Simulation approaches for burn severity estimation using remotely sensed images. *Fire Ecol.* 3 (1), 129–150.
- Cocke, A.E., Fulé, P.Z., Crouse, J.E., 2005. Comparison of burn severity assessments using Differenced Normalized Burn Ratio and ground data. *Int. J. Wildland Fire* 14 (2), 189–198. <https://doi.org/10.1071/WF04010>.
- Cohen, J.D., 2000. Preventing disaster—home ignitability in the wildland-urban interface. *J. Forest.* 98, 15–21. <https://doi.org/10.5849/jof.2017-003>.
- CONAF. (2017). Análisis de la Afectación y Severidad de los Incendios Forestales: ocurridos en enero y febrero de 2017 sobre los usos de suelo y los ecosistemas naturales presentes entre las regiones de Coquimbo y La Araucanía de Chile. [http://www.conaf.cl/tormenta\\_de\\_fuego-2017/INFORME-AFECCION-Y\\_SEVERIDAD-D E-INCENDIOS-FORESTALES-VERANO-2017-SOBRE-ECOSISTEMAS-VEGETACION-ALES-CONAF.pdf](http://www.conaf.cl/tormenta_de_fuego-2017/INFORME-AFECCION-Y_SEVERIDAD-D E-INCENDIOS-FORESTALES-VERANO-2017-SOBRE-ECOSISTEMAS-VEGETACION-ALES-CONAF.pdf).
- David Meyer, Evgenia Dimitriadou, Kurt Hornik, Andreas Weingessel, & Friedrich Leisch, 2017. e1071: Misc Functions of the Department of Statistics, Probability Theory Group (Formerly: E1071), TU Wien. <https://cran.r-project.org/package=e1071>.
- de la Barrera, F., Barrera, F., Favier, P., Ruiz, V., Quense, J., 2018. Megafires in Chile 2017: Monitoring multiscale environmental impacts of burned ecosystems. *Sci. Total Environ.* 637–638 (May), 1526–1536. <https://doi.org/10.1016/j.scitotenv.2018.05.119>.

- De Santis, A., Chuvieco, E., 2009. GeoCBI: A modified version of the Composite Burn Index for the initial assessment of the short-term burn severity from remotely sensed data. *Remote Sens. Environ.* 113 (3), 554–562. <https://doi.org/10.1016/j.rse.2008.10.011>.
- Fassnacht, F.E., Neumann, C., Forster, M., Buddenbaum, H., Ghosh, A., Clasen, A., Joshi, P.K., Koch, B., 2014. Comparison of feature reduction algorithms for classifying tree species with hyperspectral data on three central European test sites. *IEEE J. Sel. Top. Appl. Earth Obs. Remote Sens.* 7 (6), 2547–2561. <https://doi.org/10.1109/JSTARS.2014.2329390>.
- Ferreira, M.P., de Almeida, D.R.A., de Papa, D. de A., Minervino, J.B.S., Veras, H.F.P., Formighieri, A., Santos, C.A.N., Ferreira, M.A.D., Figueiredo, E.O., Ferreira, E.J.L., 2020. Individual tree detection and species classification of Amazonian palms using UAV images and deep learning. *For. Ecol. Manage.* 475 (April), 118397. <https://doi.org/10.1016/j.foreco.2020.118397>.
- French, N.H., Kasischke, E.S., Halle, R.J., Murphy, K.A., Verbyla, D.L., Hoy, E.E., Allen, J. L., 2008. Using Landsat data to assess fire and burn severity in the North American boreal forest region: an overview and summary of results. *Int. J. Wildland Fire* 17, 443–462.
- García, M., North, P., Viana-Soto, A., Stavros, N. E., Rosette, J., Martín, M.P., Franquesa, M., González-Cascón, R., Riaño, D., Becerra, J., Zhao, K., 2020. Evaluating the potential of LIDAR data for fire damage assessment: A radiative transfer model approach. *Remote Sens. Environ.*, 247, December 2019, 111893. <https://doi.org/10.1016/j.rse.2020.111893>.
- GERENCIA FORESTAL. (2011). CATASTRO DE USO DEL SUELO Y VEGETACIÓN. [https://sit.conaf.cl/tmp/obj\\_784849/268\\_Actualizacion\\_Maule\\_Biobio.pdf](https://sit.conaf.cl/tmp/obj_784849/268_Actualizacion_Maule_Biobio.pdf).
- Giglio, L., Csizsar, I., Justice, C.O., 2006. Global distribution and seasonality of active fires as observed with the Terra and Aqua Moderate Resolution Imaging Spectroradiometer (MODIS) sensors. *J. Geophys. Res. Biogeosci.* 111 (2), 1–12. <https://doi.org/10.1029/2005JG000142>.
- González, M.E., Veblen, T.T., Sibold, J.S., 2005. Fire history of Araucaria-*Nothofagus* forests in Villarrica National Park, Chile. *J. Biogeogr.* 32 (7), 1187–1202. <https://doi.org/10.1111/j.1365-2699.2005.01262.x>.
- Guo, Y., Senthilnath, J., Wu, W., Zhang, X., Zeng, Z., Huang, H., 2019. Radiometric calibration for multispectral camera of different imaging conditions mounted on a UAV platform. *Sustainability (Switzerland)* 11 (4). <https://doi.org/10.3390/su11040978>.
- Hallema, D.W., Sun, G., Caldwell, P.V., Norman, S.P., Cohen, E.C., Liu, Y., Ward, E.J., McNulty, S.G., 2017. Assessment of wildland fire impacts on watershed annual water yield: Analytical framework and case studies in the United States. *Ecohydrology* 10 (2), 1–20. <https://doi.org/10.1002/eco.1794>.
- Hamylton, S.M., Morris, R.H., Carvalho, R.C., Roder, N., Barlow, P., Mills, K., Wang, L., 2020. Evaluating techniques for mapping island vegetation from unmanned aerial vehicle (UAV) images: Pixel classification, visual interpretation and machine learning approaches. *Int. J. Appl. Earth Obs. Geoinf.* 89 (February), 102085. <https://doi.org/10.1016/j.jag.2020.102085>.
- Harvey, B.J., Andrus, R.A., Anderson, S.C., 2019. Incorporating biophysical gradients and uncertainty into burn severity maps in a temperate fire-prone forested region. *Ecosphere* 10 (2). <https://doi.org/10.1002/ecs2.2600>.
- Hoy, E.E., French, N.H., Turetsky, M.R., Trigg, S.N., Kasischke, E.S., 2008. Evaluating the potential of Landsat TM/EIM+ imagery for assessing fire severity in Alaskan black spruce forests. *Int. J. Wildland Fire* 17, 500–514.
- Hsu, C.-W., Chang, C.-C., Lin, C.-J., et al., 2003. A practical guide to support vector classification. Department of Computer Science, National Taiwan University, Tech. Rep.
- Hua, L., Shao, G., 2017. The progress of operational forest fire monitoring with infrared remote sensing. *J. For. Res.* 28 (2), 215–229. <https://doi.org/10.1007/s11676-016-0361-8>.
- Ice, G.G., Neary, D.G., Adams, P.W., 2004. Effects of Wildfire on Processes. *J. Forest.* 102 (September), 16–20.
- IUCN, 2017. IUCN Red List of Threatened Species.
- Kasischke, E.S., Bourgeau-Chavez, L.L., French, N.H., Harrell, P., Christensen, N.L., 1992. Initial observations on using SAR to monitor wildfire scars in boreal forests. *Int. J. Remote Sens.* 13 (18), 3495–3501. <https://doi.org/10.1080/01431169208904137>.
- Kattenborn, T., Hernández, J., Lopatin, J., Kattenborn, G., Fassnacht, F.E., 2018. Pilot study on the retrieval of DBH and diameter distribution of deciduous forest stands using cast shadows in UAV-based orthomosaics. *ISPRS Ann. Photogramm., Remote Sens. Spat. Inform. Sci.* 4 (1), 93–99. <https://doi.org/10.5194/isprs-annals-IV-1-93-2018>.
- Kattenborn, Teja, Eichel, J., Wiser, S., Burrows, L., Fassnacht, F.E., Schmidlein, S., 2020. Convolutional Neural Networks accurately predict cover fractions of plant species and communities in Unmanned Aerial Vehicle imagery. *Remote Sens. Ecol. Conserv.* 1–15. <https://doi.org/10.1002/rse2.146>.
- Kattenborn, Teja, Fassnacht, F.E., Schmidlein, S., 2019a. Differentiating plant functional types using reflectance: which traits make the difference? *Remote Sens. Ecol. Conserv.* 5 (1), 5–19. <https://doi.org/10.1002/rse2.86>.
- Kattenborn, Teja, Lopatin, J., Förster, M., Braun, A.C., Fassnacht, F.E., 2019b. UAV data as alternative to field sampling to map woody invasive species based on combined Sentinel-1 and Sentinel-2 data. *Remote Sens. Environ.* 227 (January), 61–73. <https://doi.org/10.1016/j.rse.2019.03.025>.
- Kattenborn, T., Schmidlein, S., 2019. Radiative transfer modelling reveals why canopy reflectance follows function. *Sci. Rep.* 9 (1), 6541. <https://doi.org/10.1038/s41598-019-43011-1>.
- Key, C.H., Benson, N.C., 2006. Landscape Assessment (LA) sampling and analysis methods. USDA Forest Service - General Technical Report RMRS-GTR, 164 RMRS-GTR.
- Kottek, M., Grieser, J., Beck, C., Rudolf, B., Rubel, F., 2006. World Map of the Köppen-Geiger climate classification updated. *Meteorol. Z.* 15 (3), 259–263.
- Kuhn, M., 2013. Predictive Modeling with R and the caret Package. <https://www.r-project.org/conferences/useR-2013/Tutorials/Kuhn.html>, useR!conference July 10–12 2013 University of Castilla-La Mancha, Albacete, Spain, 2013.
- Lentile, L.B., Holden, Z.A., Smith, A.M.S., Falkowski, M.J., Hudak, A.T., Morgan, P., Lewis, S.A., Gessler, P.E., Benson, N.C., 2006. Remote sensing techniques to assess active fire characteristics and post-fire effects. *Int. J. Wildland Fire* 15 (3), 319–345. <https://doi.org/10.1071/WF05097>.
- Lentile, L.B., Smith, A.M.S., Hudak, A.T., Morgan, P., Bobbitt, M.J., Lewis, S.A., Robichaud, P.R., 2009. Remote sensing for prediction of 1-year post-fire ecosystem condition. *Int. J. Wildland Fire* 18 (5), 594–608. <https://doi.org/10.1071/WF07091>.
- Liu, Y., Goodrick, S., Heilman, W., 2014. Wildland fire emissions, carbon, and climate: Wildfire-climate interactions. *For. Ecol. Manage.* 317, 80–96. <https://doi.org/10.1016/j.foreco.2013.02.020>.
- Lopatin, J., Fassnacht, F.E., Kattenborn, T., Schmidlein, S., 2017. Mapping plant species in mixed grassland communities using close range imaging spectroscopy. *Remote Sens. Environ.* 201, 12–23. <https://doi.org/10.1016/j.rse.2017.08.031>.
- Maier, S.W., 2010. Changes in surface reflectance from wildfires on the Australian continent measured by MODIS. *Int. J. Remote Sens.* 31 (12), 3161–3176. <https://doi.org/10.1080/01431160903154408>.
- McCarley, T.R., Kolden, C.A., Vaillant, N.M., Hudak, A.T., Smith, A.M.S., Wing, B.M., Kellogg, B.S., Kreidler, J., 2017. Multi-temporal LIDAR and Landsat quantification of fire-induced changes to forest structure. *Remote Sens. Environ.* 191, 419–432. <https://doi.org/10.1016/j.rse.2016.12.022>.
- Miller, J.D., Knapp, E.E., Key, C.H., Skinner, C.N., Isbell, C.J., Creasy, R.M., Sherlock, J. W., 2009. Calibration and validation of the relative differenced Normalized Burn Ratio (RdNBR) to three measures of fire severity in the Sierra Nevada and Klamath Mountains, California, USA. *Remote Sens. Environ.* 113 (3), 645–656. <https://doi.org/10.1016/j.rse.2008.11.009>.
- Miller, J.D., Thode, A.E., 2007. Quantifying burn severity in a heterogeneous landscape with a relative version of the delta Normalized Burn Ratio (dNBR). *Remote Sens. Environ.* 109 (1), 66–80. <https://doi.org/10.1016/j.rse.2006.12.006>.
- Morgan, P., Keane, R.E., Dillon, G.K., Jain, T.B., Hudak, A.T., Karau, E.C., Sikkink, P.G., Holden, Z.A., Strand, E.K., 2014. Challenges of assessing fire and burn severity using field measures, remote sensing and modelling. *Int. J. Wildland Fire* 23 (8), 1045–1060. <https://doi.org/10.1071/WF13058>.
- Mountrakis, G., Im, J., Ogole, C., 2011. Support vector machines in remote sensing: A review. *ISPRS J. Photogramm. Remote Sens.* 66 (3), 247–259. <https://doi.org/10.1016/j.isprsjprs.2010.11.001>.
- Mousivand, A., Verhoef, W., Menenti, M., Gorte, B., 2015. Modeling top of atmosphere radiance over heterogeneous non-Lambertian rugged terrain. *Remote Sens.* 7 (6), 8019–8044.
- Nioti, F., Dimopoulos, P., Koutsias, N., 2011. Correcting the fire scar perimeter of a 1983 wildfire using USGS-archived landsat satellite data. *GIScience Remote Sens.* 48 (4), 600–613. <https://doi.org/10.2747/1548-1603.48.4.600>.
- North, M.P., Hurteau, M.D., 2011. High-severity wildfire effects on carbon stocks and emissions in fuels treated and untreated forest. *For. Ecol. Manage.* 261 (6), 1115–1120. <https://doi.org/10.1016/j.foreco.2010.12.039>.
- Pu, R., Gong, P., Li, Z., Scarborough, J., 2004. A dynamic algorithm for wildfire mapping with NOAA/AVHRR data. *Int. J. Wildland Fire* 13 (3), 275–285. <https://doi.org/10.1071/WF03054>.
- Robichaud, P.R., Lewis, S.A., Wagenbrenner, J.W., Brown, R.E., Pierson, F.B., 2020. Quantifying long-term post-fire sediment delivery and erosion mitigation effectiveness. *Earth Surf. Proc. Land.* 45 (3), 771–782. <https://doi.org/10.1002/esp.4755>.
- Roy, D.P., Landmann, T., 2005. Characterizing the surface heterogeneity of fire effects using multi-temporal reflective wavelengh data. *Int. J. Remote Sens.* 26 (19), 4197–4218. <https://doi.org/10.1080/01431160500112783>.
- Wood, S.N., 2011. Fast stable restricted maximum likelihood and marginal likelihood estimation of semiparametric generalized linear models. *J. R. Statist. Soc. B* 73 (1), 3–36.
- Spencer, C.N., Gabel, K.O., Hauer, F.R., 2003. Wildfire effects on stream food webs and nutrient dynamics in Glacier National Park, USA. *For. Ecol. Manage.* 178 (1–2), 141–153. [https://doi.org/10.1016/S0378-1127\(03\)00058-6](https://doi.org/10.1016/S0378-1127(03)00058-6).
- Tonolli, S., Dalponte, M., Neteler, M., Rodeghiero, M., Vescovo, L., Gianelle, D., 2011. Fusion of airborne LIDAR and satellite multispectral data for the estimation of timber volume in the Southern Alps. *Remote Sens. Environ.* 115 (10), 2486–2498. <https://doi.org/10.1016/j.rse.2011.05.009>.
- Torres, D.L., Feitosa, R.Q., Happ, P.N., La Rosa, L.E.C., Junior, J.M., Martins, J., Bressan, P.O., Gonçalves, W.N., Liesenberg, V., 2020. Applying fully convolutional architectures for semantic segmentation of a single tree species in urban environment on high resolution UAV optical imagery. *Sensors (Switzerland)* 20 (2), 1–20. <https://doi.org/10.3390/s20020563>.
- Urrutia-Jalabert, R., González, M.E., González-Reyes, Á., Lara, A., Garreaud, R., 2018. Climate variability and forest fires in central and south-central Chile. *Ecosphere* 9 (4), e02171.
- Veraverbeke, S., Hook, S.J., 2013. Evaluating spectral indices and spectral mixture analysis for assessing fire severity, combustion completeness and carbon emissions. *Int. J. Wildland Fire* 22 (5), 707–720. <https://doi.org/10.1071/WF12168>.
- Verbyla, D.L., Kasischke, E.S., Hay, E.E., 2008. Seasonal and topographic effects on estimating fire severity from landsat TM/ETM+ data. *Int. J. Wildland Fire* 17, 527–534.
- Viedma, O., Chico, F., Fernández, J.J., Madrigal, C., Safford, H.D., Moreno, J.M., 2020. Disentangling the role of prefire vegetation vs. burning conditions on fire severity in a large forest fire in SE Spain. *Remote Sens. Environ.* 247 (March) <https://doi.org/10.1016/j.rse.2020.111891>.

- Weinacker, H., Koch, B., Weinacker, R., 2004. TreesVis: Treesvis-a software system for simultaneous 3d-real-time visualisation of dtm, dsm, laser raw data, multispectral data, simple tree and building models. *Int. Arch. Photogram., Remote Sens. Spat. Inform. Sci.* 36, 90–95.
- Westerling, A.L.R., 2016. Increasing western US forest wildfire activity: Sensitivity to changes in the timing of spring. *Philos. Trans. Royal Soc. B: Biolog. Sci.* 371 (1696) <https://doi.org/10.1098/rstb.2015.0178>.
- White, J.D., Ryan, K.C., Key, C.C., Running, S.W., 1996. Remote sensing of forest fire severity and vegetation recovery. *Int. J. Wildland Fire* 6 (3), 125–136. <https://doi.org/10.1071/WF9960125>.
- Whitman, E., Parisien, M.A., Thompson, D.K., Hall, R.J., Skakun, R.S., Flannigan, M.D., 2018. Variability and drivers of burn severity in the northwestern Canadian boreal forest. *Ecosphere* 9 (2). <https://doi.org/10.1002/ecs2.2128>.
- Wulder, M.A., White, J.C., Alvarez, F., Han, T., Rogan, J., Hawkes, B., 2009. Characterizing boreal forest wildfire with multi-temporal Landsat and LIDAR data. *Remote Sens. Environ.* 113 (7), 1540–1555. <https://doi.org/10.1016/j.rse.2009.03.004>.